

Model-inversion control to enforce tunable Duffing-like acoustical response on an Electroacoustic resonator at low excitation levels

E. De Bono^{a,1}, M. Morell^c, M. Collet^b, E. Gourdon^c, A. Ture Savadkoochi^c, M. Ouisse^a and C. H. Lamarque^c

^aSUPMICROTECH, Université de Franche-Comté, CNRS, institut FEMTO-ST, F-25000 Besançon, France.

^bUniv Lyon, CNRS, École Centrale de Lyon, ENTPE, LTDS, UMR5513, 69130 Ecully, France

^cUniv Lyon, ENTPE, École Centrale de Lyon, CNRS, LTDS, UMR5513, 69518 Vaulx-en-Velin, France.

ARTICLE INFO

Keywords:


nonlinear control
Duffing resonator
electroacoustic resonator
model-inversion control

ABSTRACT

The electroacoustic resonator is an efficient electro-active device for noise attenuation in enclosed cavities or acoustic waveguides. It is made of a loudspeaker (the actuator) and one or more microphones (the sensors). So far, the desired acoustic behaviour, expressed in terms of a linear-time-invariant relationship between sound pressure and vibrational motion (the acoustical impedance), has been more efficiently achieved by a model-inversion strategy which is implemented by driving the electrical current in the loudspeaker coil, based upon the measured pressure. The corrector transfer function is defined in the Laplace domain and digitally executed by the classical infinite-impulse-response technique, though a state-space representation could be employed. In this work, we are interested in enforcing a nonlinear behaviour at low sound excitation levels, where the electroacoustic resonator would normally behave as a linear-time-invariant system. Hence, in order to transform its acoustical response from linear to nonlinear, the model-inversion technique must be reformulated in time domain. The state-space representation of the relationship between the input measured pressure and the output electrical current gives the right perspective and the solution to this problem. We provide the conception of this model-inversion control algorithm capable of transforming a linear-time-invariant acoustical response to potentially any causal acoustical response of the electroacoustic resonator. Such control strategy is tested by targeting a Duffing acoustical response with tunable parameters. Both numerical simulations and experimental tests in quasi-open field validate the approach. The results provided in this contribution open the doors for conceiving non-conventional absorbers which can exploit nonlinear phenomena for noise mitigation even at low excitation amplitudes.

1. Introduction

The wave-control by treating the boundaries of propagative domains is a large area of research encompassing all fields from electromagnetics to solid mechanics and acoustics. In acoustics, a typical boundary treatment problem is the room modal damping, where the objective is to damp the acoustic modes in an enclosed cavity. Morse [1] recognized the normal surface impedance as the quantity characterizing the acoustic behaviour of a locally reacting boundary, in its *linear regime*. It is defined as the ratio of Laplace transform of the local sound pressure and the normal velocity: $Z_s(s) = p(s)/v(s)$, where s is the Laplace variable, set to $j\omega$ (where $j = \sqrt{-1}$) in the stationary regime. However, a generic boundary might present non-locally reacting, non-linear or even time-variant acoustical response, and can be characterized by a general operator $\mathcal{L}\{p(\mathbf{x}, t), \mathbf{u}(\mathbf{x}, t), t\} = 0$, relating sound pressure p and the surface displacement \mathbf{u} in the physical coordinates (\mathbf{x}, t) . In case of locally-reacting and linear time-invariant (LTI) behaviour of the boundary, the implicit general operator $\mathcal{L}\{\bullet\}$ degenerates to a LTI relationship between local sound pressure $p(t)$ and normal velocity $v(t)$, whose Laplace or Fourier transform leads to the definition of the normal surface impedance: $p(s) - Z_s(s)v(s) = 0$. Though the linear regime is valuable only below a certain threshold of the involved energy, both in acoustics and solid mechanics the problem of noise and vibration mitigation has been mostly tackled by LTI means. In solid mechanics, the Tuned-Vibration-Absorber (TVA) [2], consists of a resonator attached to the main structure, properly tuned with the resonance of the primary structure (supposed linear). Nevertheless, since mistuned TVA might increase the vibration level of the primary structure, *adaptive* TVAs [2] have been developed with controllable or adjustable parameters, as well as *active* TVAs. The active TVAs, thanks to an *active* force on the mass, can provide broader bandwidth, and

 emanuele.bono@femto-st.fr (E. De Bono)

ORCID(s):

when the active element fails, they can still function as passive vibration absorbers (fail-safe).

The resonance principle of energy capture is also exploited in sound mitigation by the Helmholtz or quarter-wavelength resonators, which are equivalent to TVAs in solid mechanics. Their main drawback is the fact that the equivalent acoustical stiffness term is related to the air compressibility in their acoustic cavity. Hence, to target lower frequencies, larger volumes of air are required, limiting their implementation when confronted with space and weight strict specifications, as in aeronautics for example [3]. Also the Helmholtz and quarter-wavelength resonators have found some evolution by *adaptive* solutions for coping with tunability requirements [3]. Other classical passive acoustic resonators are membranes, which are also exploited in (electro)-*active* devices, such as the so-called Electroacoustic Resonators (ER). As in the active TVA, a *control* force is applied to the mass of the ER which can modify its response to the acoustic excitation. Most commonly used technology for the ER is the loudspeaker, where the dynamics of the speaker membrane is altered by the Lorentz/Laplace control force. From the seminal idea of Olson and May [4], the ER concept has given rise to various strategies, such as electrical-shunting [5], direct-impedance control [6] and self-sensing [7]. In order to overcome the low-flexibility drawback of electrical shunting techniques, minimize the number of sensors, meanwhile avoiding to get involved into the electrical-inductance modelling of the loudspeaker, a pressure-based current-driven architecture proved to achieve the best absorption performances in terms of both bandwidth and tunability [8]. It employs one or more pressure sensors (microphones) nearby the speaker, and a model-inversion technique to target the desired impedance by controlling the electrical current in the speaker coil. Its efficiency has been demonstrated for room-modal equalization [9], sound transmission mitigation in waveguides [10], [11], and even non-reciprocal propagation [12].

In solid mechanics, it has long been tried to overcome the limits of linear TVA by exploiting non-linear (typically Duffing type) resonators [13], [14]. In early 21st century, it has been demonstrated that the coupled dynamics of the linear main structure and nonlinear absorber, can feature a special phenomenon: the Targeted Energy Transfer (TET) where vibrational energy is transferred from the linear host structure to the nonlinear absorber in a one-way and irreversible fashion [15], [16]. A widely used device presenting TET is the Nonlinear-Energy-Sink (NES) [17]. The NES is largely studied in solid mechanics, in its different forms, such as pure cubic [16] or non-smooth [18]. In acoustics, the potentialities of nonlinear sound absorption have been explored in [19] for designing Helmholtz resonators in the nonlinear regime, or in [20], where TET was achieved from a linear acoustic cavity to a *weakly-coupled* thin visco-elastic membrane which behaves as a Duffing resonator. As the linear ones, passive nonlinear absorbers are not easily tunable for targeting different bandwidths. Moreover, they usually need high-energy threshold in order to trigger the nonlinear behaviour. An electro-active nonlinear absorber might overcome these limitations, by *transforming* the mechano-acoustical dynamics of the loudspeaker from linear to nonlinear, while keeping the same external excitation levels. In order to do that, in [21], an additional microphone was placed inside the ER back-cavity, such that to retrieve a measurement directly proportional to the diaphragm displacement at low frequencies. The nonlinear behaviour was then induced by defining an electrical current (the controller) which comprises a “linear” (i_L) and a “nonlinear” (i_{NL}) contribution separately. While i_L is in charge of inverting the loudspeaker own dynamics and enforcing the linear part of the target dynamics, i_{NL} is in charge of enforcing the nonlinear term, proportional to the cubic pressure inside the back-cavity of the EA. To apply this strategy, attention must be put in the recursive definition of the “linear” term i_L in its digital implementation. In the classical Infinite-Impulse-Response (IIR) recursive scheme [22], the controller at each time step is defined based upon its value at the previous time steps. Hence, in order for i_L to correctly accomplish the model-inversion and the “linear” dynamics targeting, in the IIR scheme, i_L should never be mixed up with i_{NL} in [21]. The nonlinear behaviour accomplished by this device, manifesting itself in the *hardening* or *softening* spring effects, is mildly evident in [21] as a small enlargement of the bandwidth with respect to the purely linear control. The great achievement of [21] though, was to be able of *adding* a nonlinear term to the LTI dynamics of the EA, at relatively low excitation levels. This was accomplished by increasing the gain multiplying the sensed pressure in the back-cavity, which was however limited by important stability constraints. Moreover, difficulties would arise for this strategy, based upon the separation of the *linear* (i_L) and *nonlinear* (i_{NL}) contributions, if it should be implemented to target *multi-degree-of-freedom* (MDOF) nonlinear dynamics.

In this paper we write the model-inversion control problem to transform the acoustical response of the electroacoustic resonator (ER) from LTI to potentially any causal locally-reacting response (nonlinear and/or time-variant), in the same pressure-based, current-driven architecture of [8], without additional sensors to estimate the motion of the speaker membrane. For non-LTI target dynamics, the control problem must be written in time domain. The state-space representation gives the right perspective to formulate the algorithm. In the algorithm proposed here, the non-LTI dynamics is integrated by a numerical scheme at each time step, in order to retrieve the target state-vector from the

sensed variable (the sound pressure). The computed target state-vector is hence inserted in the model of the ER system to get the electrical current (the controller) capable of enforcing the desired dynamics. In this contribution, the control algorithm is implemented to achieve a Duffing-like acoustical behaviour, with tunable parameters. The novelty of this contribution consists in presenting a control technique capable of enforcing linear as well as nonlinear dynamics, as it is not conceived from a convolution filter, moreover without requiring additional displacement sensors. The innovation stays indeed in employing a Runge-Kutta-like scheme for integrating in real-time the target dynamics, and synthesizing a model inversion controller in real time. This work opens the doors to investigate the potentialities of various non-LTI absorbers, and to the *inverse design* of ad-hoc non-LTI operators for the scope of wave control at low excitation levels. In Section 2, the model-inversion strategy is outlined for a general non-LTI target acoustical response. In Section 3, the approach is numerically validated by simulating the acoustical response of the controlled system in open-field, for both linear and nonlinear (Duffing) target dynamics. In Section 4, the strategy is implemented on an experimental prototype, and measurements in a quasi-open field are carried out to validate the achievement of a tunable Duffing-like response of the ER at low excitation levels. Finally, in Section 5, we give the conclusions and future developments.

2. Model-inversion control concept

In this section we provide the general concept of model-inversion control, from which the strategy to transform the ER dynamics from LTI to generic non-LTI, stems from. For convenience, we formulate the problem directly in the case of our ER, but it could be easily translated to other kinds of control systems. The model-inversion approach starts with the definition of a desired target behaviour [23], which in our case is the acoustical response of the ER as a general (possibly non-LTI) operator relating sound pressure on the speaker diaphragm, and vibrational motion of the ER mass. In state-space it can be written as: $\dot{\mathbf{x}}_d(t) = f_d(\mathbf{x}_d(t), p_d(t), t)$, where f_d is the N -order differential operator of the *desired* dynamics, $\mathbf{x}_d(t)$ is the *desired* state-vector comprising the displacement and its time derivatives up to the order $N - 1$, and $p_d(t)$ is the *desired* sound-pressure. To achieve such target behaviour, the model-inversion approach synthesizes the control variable (in our case the electrical current $i(t)$) based upon the assumption of the system model. In our case the model is the relationship between sound pressure, control force applied on the ER mass, and vibrational motion of ER mass: $p(t) = g_m(\mathbf{x}(t), i(t))$, where g_m is the system-model differential operator, $\mathbf{x}(t)$ is the actual ER state-vector, and the control force is expressed as function of the electrical current $i(t)$ as it pilots the electromagnetic force produced in the speaker coil. The two equations are grouped together in Eq. (1).

$$\begin{cases} \dot{\mathbf{x}}_d(t) = f_d(\mathbf{x}_d(t), p_d(t), t), \\ p(t) = g_m(\mathbf{x}(t), i(t)). \end{cases} \quad (1a)$$

$$\quad \quad \quad (1b)$$

In our case, $g_m(\bullet)$ is a LTI differential operator, while $f_d(\bullet)$ can be a non-LTI differential operator. The controller, i.e. the electrical current $i(t)$, which is capable of *transforming* the ER dynamics from Eq. (1b) to Eq. (1a), is the solution of the system of Eq.s (1), for $\mathbf{x}(t) = \mathbf{x}_d(t)$ and $p(t) = p_d(t)$.

The architecture at disposal allows to estimate the actual $p(t)$ by one or more microphones, hence in Eq. (1) we can take $p_d(t) = p(t)$.

Let us first consider the case of a more familiar LTI target operator $f_d(\bullet)$. In this case, both Eq. (1a) and Eq. (1b) are LTIs systems, and can be rewritten in matrix notation:

$$\begin{cases} \dot{\mathbf{x}}_d(t) = A\mathbf{x}_d(t) + Bp(t), \\ p(t) = C_1\dot{\mathbf{x}}(t) + C_2\mathbf{x}(t) + D_1i(t), \end{cases} \quad (2a)$$

$$\quad \quad \quad (2b)$$

where A , B , C_1 , C_2 and D_1 are constant matrices. In order to find the control output $i(t)$ as function of the input $p(t)$, we simply have to impose $\mathbf{x}(t) = \mathbf{x}_d(t)$. By doing so, Eq. (2b) can be rewritten in the classical form of state-space LTI systems:

$$p(t) = C\mathbf{x}_d(t) + Di(t), \quad (3)$$

with $C = (1 - C_1B)^{-1}(C_1A + C_2)$ and $D = (1 - C_1B)^{-1}D_1$. From Eq.s (2a) and (3) we are used to get the corrector transfer function between the input $p(t)$ and the output $i(t)$, in the Laplace variable s :

$$H(s) = \frac{i(s)}{p(s)} = D^{-1}[1 - C(sI - A)^{-1}B] \quad (4)$$

Observe that if we compute the state-space representation of the filter $H(s)$, we would retrieve the system of Eq.s (2). This observation provides an interesting interpretation of state-space representations, from a *model-inversion perspective*: the first equation of the state space representation would describe the target dynamics, and the second one the system model.

For its digital implementation, the corrector transfer function $H(s)$ is transformed in the discrete Laplace space z by a zero-order-holder (zoh) or Tustin transform [22]. Such transformations allow to approximate the convolution integral $i(t) = \int_0^t H(t)p(t - \tau)d\tau$ by a finite sum of lower rectangles (zoh) or trapezoids (Tustin), hence to obtain the controller $i(t)$ at each time step. This is the classical convolution approach, for the design of the model-inversion control as in [8].

A non-LTI target dynamics does not allow the passage to the Laplace domain and the direct definition of the corrector $H(s)$. Nevertheless, the state-space representation of Eq.s (1), allows for another solution to enforce possibly non-LTI desired dynamics in a LTI system. For clarity, the system of equations is rewritten in Eq.s (5) to specify that the target dynamics can be non-LTI, while the system model is LTI and can, therefore, be directly *inverted*.

$$\begin{cases} \dot{\mathbf{x}}_d = f_d(\mathbf{x}_d(t), p(t), t), \\ p(t) = C_1 \dot{\mathbf{x}}(t) + C_2 \mathbf{x}(t) + D_1 i(t). \end{cases} \quad (5a)$$

$$\quad (5b)$$

At each time step t_n of the digital implementation, we can retrieve the target state-vector $\mathbf{x}_d(t_{n+1})$ based upon the measured pressure $p(t_n)$, by solving Eq. (5a) thanks to a numerical scheme. Then, we impose $\mathbf{x}(t_{n+1}) = \mathbf{x}_d(t_{n+1})$ in Eq. (5b), in order to retrieve $i(t_{n+1})$. The digital implementation strategy just proposed, essentially consists of two steps, illustrated below:

1. Evaluate $\dot{\mathbf{x}}_d(t_n) = f_d(\mathbf{x}_d(t_n), p(t_n), t_n)$, from the measured pressure $p(t_n)$ and the state vector $\mathbf{x}_d(t_n)$ estimated at the previous time step. Then, inject the controller $i(t_n)$ obtained by *inverting* Eq. (5b):

$$i(t_n) = D_1^{-1}[p(t_n) - C_1 \dot{\mathbf{x}}_d(t_n) - C_2 \mathbf{x}_d(t_n)] \quad (6)$$

2. Apply an integration scheme to $\dot{\mathbf{x}}_d(t_n) = f_d(\mathbf{x}_d(t_n), p(t_n), t_n)$ and estimate the target state vector $\mathbf{x}_d(t_{n+1})$ for the next step.

Such control algorithm will be labelled as Real-Time-Integration (RTI) to differentiate it from the IIR implementation of the convolution-based algorithms. Notice that the RTI allows to *transform* the system acoustical dynamics (given by the relationship between $p(t)$ and $\mathbf{x}(t)$) from LTI to non-LTI, while classical convolution-algorithms do not permit the modification of the nature (LTI or non-LTI) of the original system.

Fig. 1 shows the block diagram of the two-steps control algorithm described above. The z^{-1} block in Fig. 1 follows the symbolism of the Simulink toolbox of Matlab to indicate that the desired state vector, computed at time step t_n , is employed in the controller i at the next time step $t_n + 1$.

Different choices can be made for the integration scheme employed to solve Eq. (5a). For example, a proper Runge-Kutta scheme of fourth order (RK4) would require the pressure p to be measured at the multiple instants t_n , $t_n + h/2$ and $t_n + h$, with h being the time step of the integration. In order to do that, the acquisition rate (control input) should be twice the sampling frequency of the digital control output ($i(t)$ and $p(t)$ should have different sampling frequencies). Calling $f_s = 1/T_s$ the maximum sampling frequency of our digital control, a proper RK4 integration scheme can be obtained by considering $h = 2T_s$. This way, the acquisition sampling rate would be set to f_s , while the controller rate would be $f_s/2$. The numerical integration scheme employed in this contribution, presents a fixed sampling rate for both the input p and the output i of the control, with integration step $h = T_s$. This choice, does not allow to implement a proper RK4 integration scheme, as the sound pressure p is unknown at the intermediate stages. Nevertheless, the pressure p can be considered as constant at the intermediate steps of integration of Eq. (5a), while the increments of

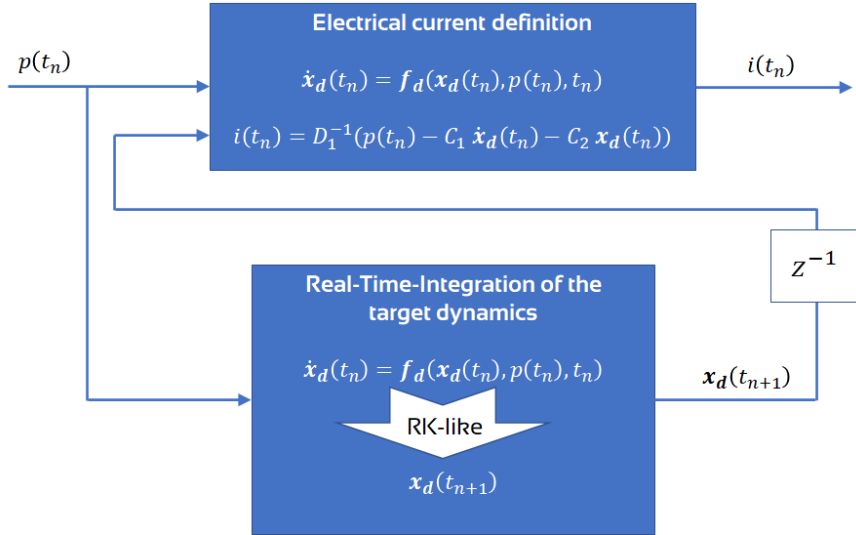


Figure 1: Block diagram of the two-steps control algorithm.

the unknown vector \mathbf{x}_d can be computed following the typical RK4 scheme. In this case, we cannot speak of a proper RK algorithm, but of a RK-like scheme. Nonetheless, thanks to a high sampling rate of 50 kHz, keeping the pressure unchanged at the intermediate stages of the RK scheme does not threaten the accuracy of integration, while allowing to acquire the pressure signals at the fastest rate. In the following sections, the accuracy of such integration scheme is assessed by comparison with the results and errors of classical IIR convolution algorithms, both numerically and experimentally.

Observe also that, as for any digital implementation, this control entails a physiological time-delay τ between the input and output [24], meaning that in Eq. (6) a $p(t_n - \tau)$ is actually taken into account, and not $p(t_n)$.

In the next section, we numerically simulate the implementation of such control algorithm applied on an ER, in an open-field acoustic environment.

3. Numerical validation

In this section we simulate the implementation of the RTI digital control algorithm described in Section 2, on an ER placed in an open-field environment. So, let us first describe the physical problem. An open-field environment means that the ER is placed on the boundary of a semi-infinite domain. An incident sound wave impacts the ER diaphragm and a reflected wave is produced, as illustrated in Fig. 2. Hence, there is *no-coupling* between the ER and the surrounding, i.e. the acoustic field is composed by the superposition of incident and reflected propagating plane waves, which do not interact with each other except at the ER diaphragm. This simplified context allows to analyse the response of the controlled ER alone, without any *coupling* effects with external acoustic modes, the latter being a critical aspect especially for nonlinear resonators, and deserves a dedicated discussion which will be carried out in a following paper.

In Fig. 2, the ER is placed on the boundary $\partial\Omega$ of a 2-dimensional (2D) semi-infinite acoustic domain Ω . On the ER interface with the semi-infinite domain an incident plane wave p^+ impacts on the ER with an incidence angle θ . Consequently, a reflected plane wave field p^- is produced at the interface. The relationship between the ER displacement and the incident and reflected sound pressure waves, is given by the linearised conservation of momentum [25]:

$$-\rho_0 \ddot{u}(t) = \partial_x p(x, y, t), \quad \text{on } x = 0 \quad (7)$$

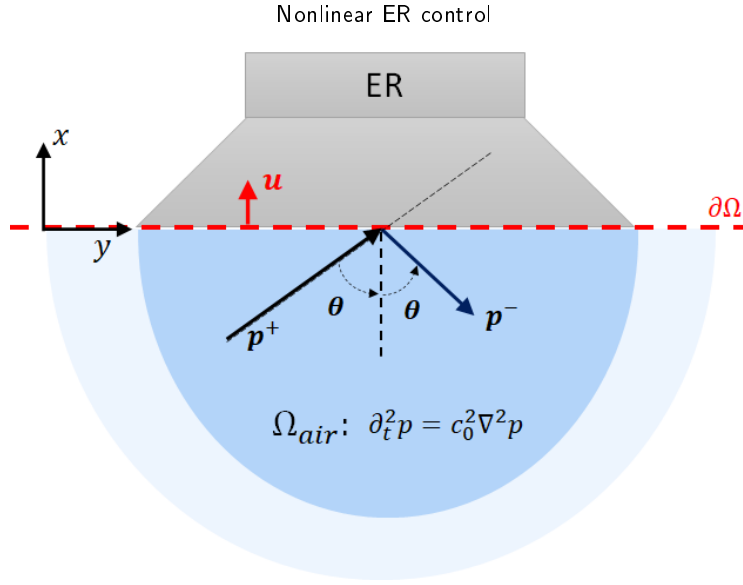


Figure 2: ER interfacing with a semi-infinite acoustic domain.

where ρ_0 is the static air-density, $u(t)$ is the displacement of the ER, the upper dot indicating the time derivative, 208
and $p(x, y, t)$ is the sound pressure. The sound pressure $p(x, y, t)$ can be written in terms of incident p^+ and reflected 209
 p^- plane waves: 210

$$p(x, y, t) = p^+(x \cos \theta - c_0 t, y \sin \theta - c_0 t) + p^-(x \cos \theta + c_0 t, y \sin \theta - c_0 t). \quad (8)$$

Hence, Eq. (7) becomes: 211

$$\begin{aligned} \ddot{u}(t) &= \frac{\cos \theta}{\rho_0 c_0} \left(\partial_t p^+(t) - \partial_t p^-(t) \right) \\ \Rightarrow \dot{u}(t) &= \frac{\cos \theta}{\rho_0 c_0} \left(p^+(t) - p^-(t) \right), \end{aligned} \quad (9)$$

where c_0 is the sound speed, $p^+(t)$ and $p^-(t)$ are the incident and reflected fields at the interface, with the y 212
dependence dismissed because we are interested in the *local reaction*. Let us now write our ER model equation, 213
according to the Single-Degree-of-Freedom (SDOF) approximation of the loudspeaker mechano-acoustical dynamics: 214

$$M_{a0} \ddot{u}(t) + R_{a0} \dot{u}(t) + K_{a0} u(t) = p(t) - \frac{Bl}{S_e} i(t), \quad (10)$$

where M_{a0} , R_{a0} and K_{a0} are the acoustical mass, resistance and stiffness of the loudspeaker in open circuit, while 215
 Bl is the force factor (magnetic field times the coil length) and S_e is the equivalent piston area, of the ER [26]. Observe 216
that we have labelled $p(t)$ the sound pressure applied on the speaker membrane, supposed to be uniform (independent of 217
 y) at sufficiently low frequencies respect to the dimensions of the speaker diaphragm. By definition of a *locally-reacting* 218
boundary, the sound pressure can be considered uniform on each element of the (discretized) boundary [27, 28, 3], so 219
that the behaviour of locally-reacting boundaries can be described by their *local impedance*. This is true for wavelengths 220
sufficiently larger than the lateral size of the boundary element. Moreover, in the experimental EA prototype employed 221
in Section 4, the pressure input around the speaker is averaged, making the *local impedance* assumption effective up to 222
around 2 kHz [12, 29, 11] in the *average* sense. Clearly, at higher frequencies, the average *locality* fails and spillover 223
effects might arise. This drawback, along with the time delay of the digital control, limits the controllability of our ER 224
[24]. At sufficiently low frequencies, then, on the speaker interface $p(y, t) \approx p(t) = p^+(t) + p^-(t)$. 225
In Fig. 3, the SDOF model is illustrated in terms of the mechanical parameters $(\bullet)_{m0} = (\bullet)_{a0} S_e$. 226

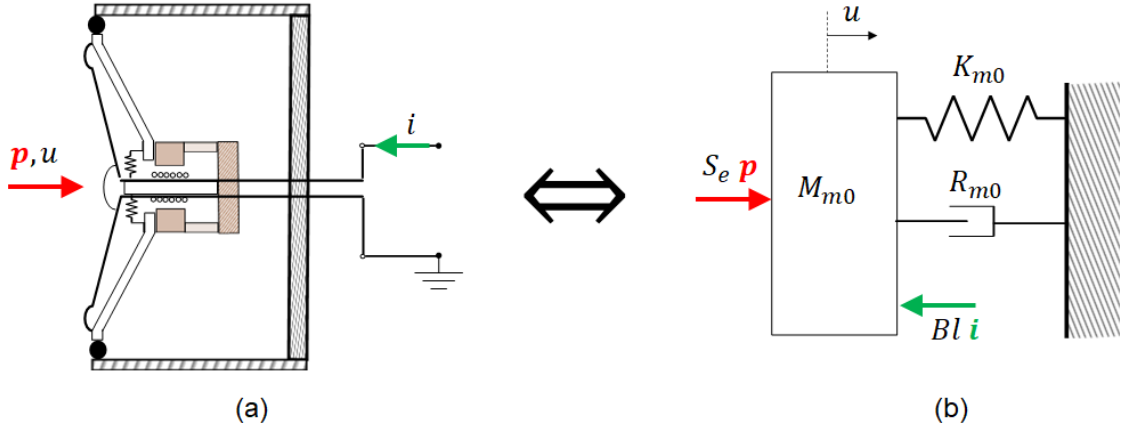


Figure 3: Sketch of the ER (a) and its SDOF piston-mode model (b) employed in the control synthesis.

Defining the state-space vector $\mathbf{x}(t) = [u(t), \dot{u}(t)]$, Eq. (5b) rewrites:

$$p(t) = [R_{a0}, M_{a0}] \dot{\mathbf{x}}(t) + [K_{a0}, 0] \mathbf{x}(t) + \frac{Bl}{S_e} i(t), \quad (11)$$

where we can recognize the matrices C_1 , C_2 and D_1 of Eq. (5b), and $i(t)$ is obtained at each time step by the algorithm defined in Section 2. As we know, our control aims at targeting a specific operator relating local sound pressure $p(t)$ (input) and membrane vibration (actuator response $\mathbf{x}(t)$). Nevertheless, the local sound pressure $p(t)$ depends, in turn, upon the system response itself $\mathbf{x}(t)$, according to the external acoustic environment where the ER is placed. In the Laplace/Fourier domain, it is the so-called *radiation impedance* [26], which operates like an acoustic feedback on the boundary [24]. This equation defines the acoustical environment where the ER is placed. Observe that such relationship cannot be retrieved by our ER local sensors, hence it cannot directly affect the target operator synthesis. To properly assess and predict the performances of any acoustical device by numerical simulations, though, such equation should be taken into account in the problem simulation. This means that the control input $p(t)$ should not be considered as an independent term (as it were a source, as it is done in [21]), but it should be written in terms of the system response $\mathbf{x}(t)$, the latter providing the scattering of sound waves. Indeed, Eq. (11) describes a so-called non-ideal system [30], in the sense that the local sound pressure $p(t)$ depends upon the response of the system itself $\mathbf{x}(t)$. In an open-field environment, the relationship between $p(t)$ and $\mathbf{x}(t)$ is given by Eq.s (8) and (9), i.e.:

$$p(t) = 2p^+(t) - [0, \rho_0 c_0 / \cos \theta] \dot{\mathbf{x}}(t). \quad (12)$$

Hence, inserting Eq. (12) in Eq. (11), we obtain the following equation relating the source term $p^+(t)$ and the state vector $\mathbf{x}(t)$:

$$2p^+(t) = \left[R_{a0} + \frac{\rho_0 c_0}{\cos \theta}, M_{a0} \right] \dot{\mathbf{x}}(t) + \left[K_{a0}, 0 \right] \mathbf{x}(t) + \frac{Bl}{S_e} i(t). \quad (13)$$

For what explained above concerning the *non-ideality* of the system, the assumption of [21] of $p(t)$ as a fixed source term in simulations, is incorrect. In an open field environment simulation, since the incident and scattered fields do not interact with each other (except at the interface with the boundary), we can fix $p^+(t)$ at all instants (as a known source term) and find the time-evolution of $\mathbf{x}(t)$ by numerically solving Eq. (13) at each time step t_n . The electrical current $i(t_n)$ in Eq. (13) is retrieved at the previous time step from Eq. (6). Once the state vector at the next time step $\mathbf{x}(t_{n+1})$ is known, the total sound pressure $p(t_{n+1})$ is computed from Eq. (12) (where p^+ is known at all instants). Hence, $p(t_{n+1})$ can be fed into the control algorithm of Fig. 1, to find the controller $i(t_{n+1})$, and the recursive simulation goes on. Notice that a time-delay τ can also be simulated, by taking into account $p(t_n - \tau)$ in the control Eq. (6).

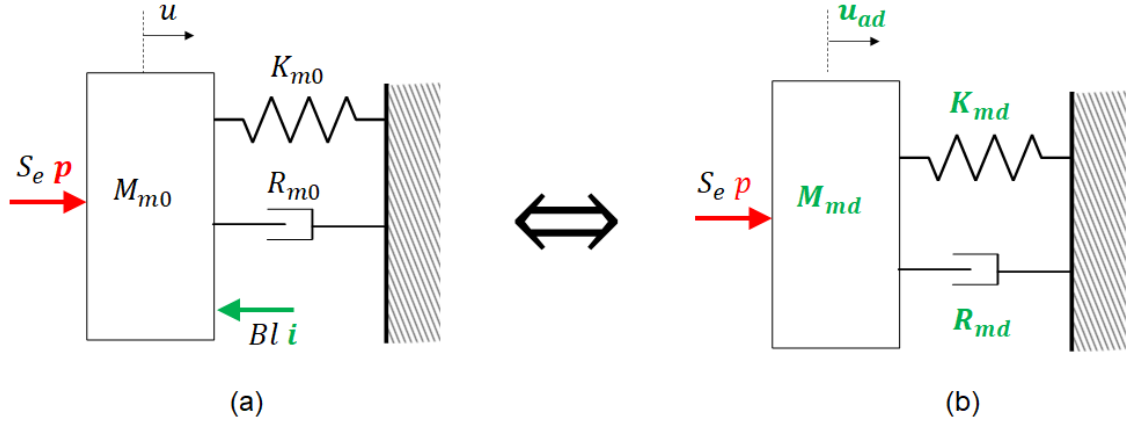


Figure 4: Sketches of the SDOF model of the ER (a) and of the target SDOF LTI resonator (b).

3.1. Linear target dynamics

In order to compare the performances of the RTI versus the classical IIR algorithm, let us first consider a linear SDOF target dynamics (as in [8, 10, 12, 24, 11]). The desired behaviour is described by:

$$M_{ad}\ddot{u}_d(t) + R_{ad}\dot{u}_d(t) + K_{ad}u_d(t) = p(t), \quad (14)$$

where M_{ad} , R_{ad} and K_{ad} are the desired acoustic mass, resistance and stiffness of the ER target acoustical dynamics, and $u_d(t)$ is the corresponding desired displacement. In Fig. 4, the target SDOF dynamics is illustrated in terms of the mechanical parameters $(\bullet)_{md} = (\bullet)_{ad} S_e$.

In [8] the desired mass and stiffness are defined in terms of the open-circuit values $M_{ad} = \mu_M M_{a0}$ and $K_{ad} = \mu_K K_{a0}$, and the resistance is represented as a fraction of $\rho_0 c_0$. The desired resonance frequency can then be expressed in terms of the open-circuit one $f_d = \sqrt{\frac{\mu_K}{\mu_M}} f_0$, with $f_0 = \frac{1}{2\pi} \sqrt{\frac{K_{a0}}{M_{a0}}}$. In what follows, the open-circuit acoustical mass, resistance and stiffness of the ER are taken equal to $M_{a0} = 0.392 \text{ kg.m}^{-2}$, $R_{a0} = 194 \text{ Pa.s.m}^{-1}$ and $K_{a0} = 4.25 \times 10^6 \text{ Pa.m}^{-1}$ respectively, which brings an $f_0 \approx 525 \text{ Hz}$. These values are the same as the ones identified for the experimental prototype analysed in Section 4.

In this section, the open-field problem in case of normal incidence is simulated in time by a RK4 algorithm, both in case of IIR and RTI control algorithms. For harmonic incident waves $p^+(t)$, the reflection and hence absorption $\alpha_n(\omega)$ coefficients spectra can be retrieved by taking the Discrete-Fourier-Transform (DFT) of the incident and reflected signals.

In Fig. 5 the time histories of the reflected pressure $p^-(t)$, electrical current $i(t)$, and ER velocity for harmonic incident pressure $p^+(t)$ at 500 Hz and amplitude 1 Pa, are presented in case of IIR and RTI control strategies. The time histories for IIR and RTI are indistinguishable. In Fig. 6, we show the normal absorption coefficients $\alpha_n(\omega)$ retrieved computing the DFT of the incident and reflected pressures signals, in case of IIR and RTI control implementation, as well as the curve of $\alpha_n(\omega)$ obtained directly from the Frequency-Response-Functions (FRFs) of the ER acoustical mobility. The FRFs though, are here evaluated by taking the Tustin transform [22] of the discrete corrector $H(z)$ in order to obtain $H(s)$, so that the transfer function $H(s)$ (i.e. $H(j\omega)$) be equivalent to $H(z)$ in the sense described in [22]. The target acoustical dynamics has $\mu_M = \mu_K = 1$ and $R_{ar} = \rho_0 c_0$.

The two implementation strategies (IIR or RTI) look equivalent both in Fig. 5 and 6. Fig. 6 shows that the RK4 algorithm employed for the simulation of the normal incidence problem in time domain, produces a phase-shift due to numerical errors, which grows up in frequency. Indeed, such a phase shift is present independently of delayed or perfectly synchronized controllers, as showed in Fig. 6. Therefore, the loss of acoustical passivity displayed by $\alpha_n(\omega)$ from 2 kHz and above, is related to truncation errors of the numerical scheme, which is more important as the frequency increases, for a fixed time resolution. In the simulation result of Fig. 6b, the time delay has been considered equal to

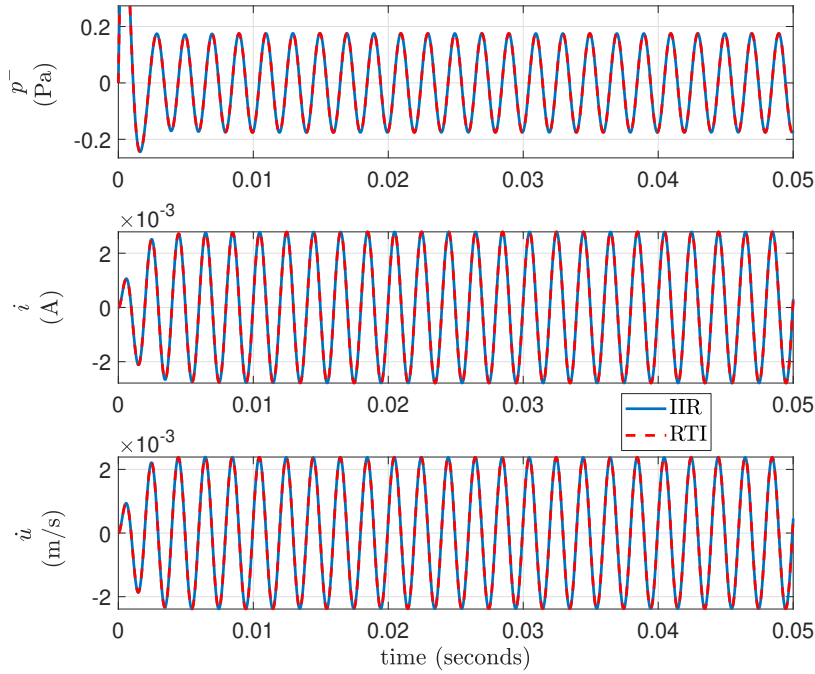


Figure 5: Simulated time histories of ER velocity $\dot{u}(t)$, reflected pressure $p^-(t)$ and electrical current signals $i(t)$, for harmonic normally-incident pressure wave $p^+(t)$ of amplitude 1 Pa at 500 Hz, in case of IIR (in solid blue) and RTI (in dashed red) controller implementations.

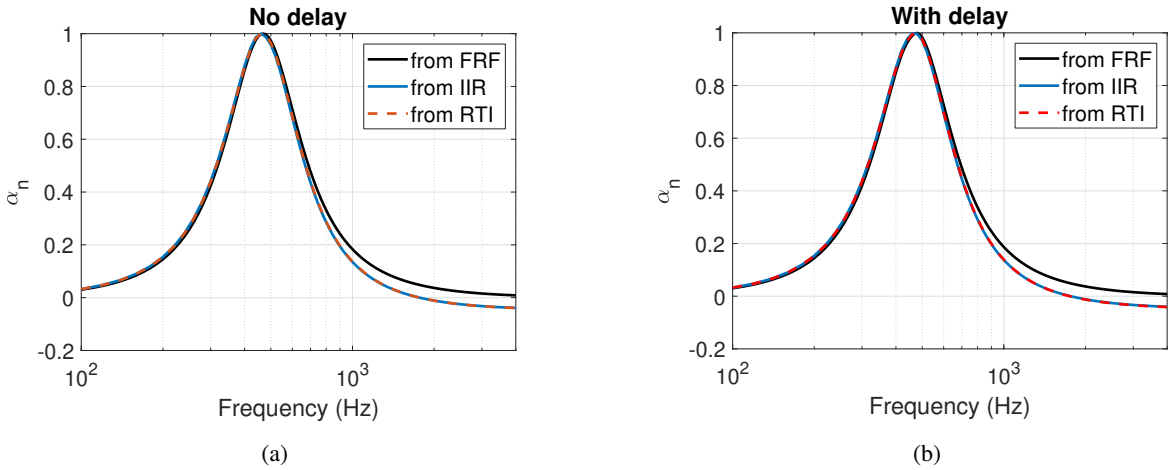


Figure 6: Simulated normal absorption coefficients obtained directly in frequency domain from $H(j\omega)$ (in black) compared with the values obtained by the IIR (in blue) and RTI (in dashed red) time implementations of the controller. In (a) no time delay is assumed, while in (b) a time delay of 2×10^{-5} seconds is considered. The target impedance operator is set with values: $\mu_M = \mu_K = 1$ and $R_{at} = \rho_0 c_0$.

2×10^{-5} seconds as in [8].

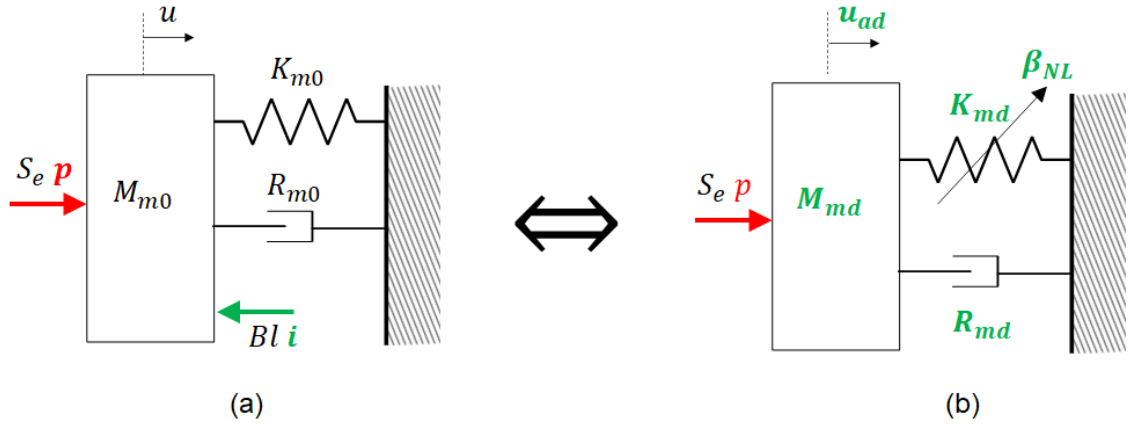


Figure 7: Sketches of the SDOF model of the ER (on the left) and of the target SDOF Duffing resonator (on the right).

3.2. Duffing-type target dynamics

Once the equivalence of the RTI algorithm with the classical IIR one, has been numerically demonstrated, we can now investigate on the implementation of a cubic (Duffing-type) target dynamics, as the one in Eq. (15):

$$p(t) = M_{ad}\ddot{u}_d(t) + R_{ad}\dot{u}_d(t) + K_{ad}\left(u_d(t) + \beta_{NL}u_d^3(t)\right), \quad (15)$$

where the coefficient β_{NL} multiplies the cubic of the target displacement $u_d^3(t)$, and has therefore the dimensions of m^{-2} .

Fig. 7 shows the SDOF model of the ER employed by the model inversion strategy described in Section 2, to target a SDOF Duffing resonator sketched on Fig. 7b.

Same open field problem is considered with normally incident harmonic sound wave $p^+(t) = p_0^+ \sin(\Omega t)$. The frequency Ω of the harmonic signal $p^+(t)$ is varied in order to get the spectra.

The time-histories, along with its DFTs in case of $\mu_M = \mu_K = 1$, $R_{at} = \rho_0 c_0$ and $\beta_{NL} = 1 \times 10^{13} m^{-2}$ are reported in Fig. 8 and Fig. 9, for incident harmonic pressure wave with $\Omega = 2\pi 700$ Hz. Fig. 8a clearly shows a multi-harmonic response of the ER, due to the electrical current. In Fig. 8b the third harmonic (at $2100 = 700 \times 3$ Hz), typical of the Duffing resonator response [30], is evident. Moreover, Fig. 8 presents the simulation results in case of time delay $\tau = 0$ and $\tau = 2 \times 10^{-5}$ seconds simulated in the digital control implementation. Fig. 9 zooms the velocity time histories in the stationary regime and the DFT around the fundamental frequency. From Fig. 9, the effect of time delay is clearly visible in detaching the actual velocity \dot{u} from the desired one \dot{u}_d , both in the time history and in the frequency spectrum.

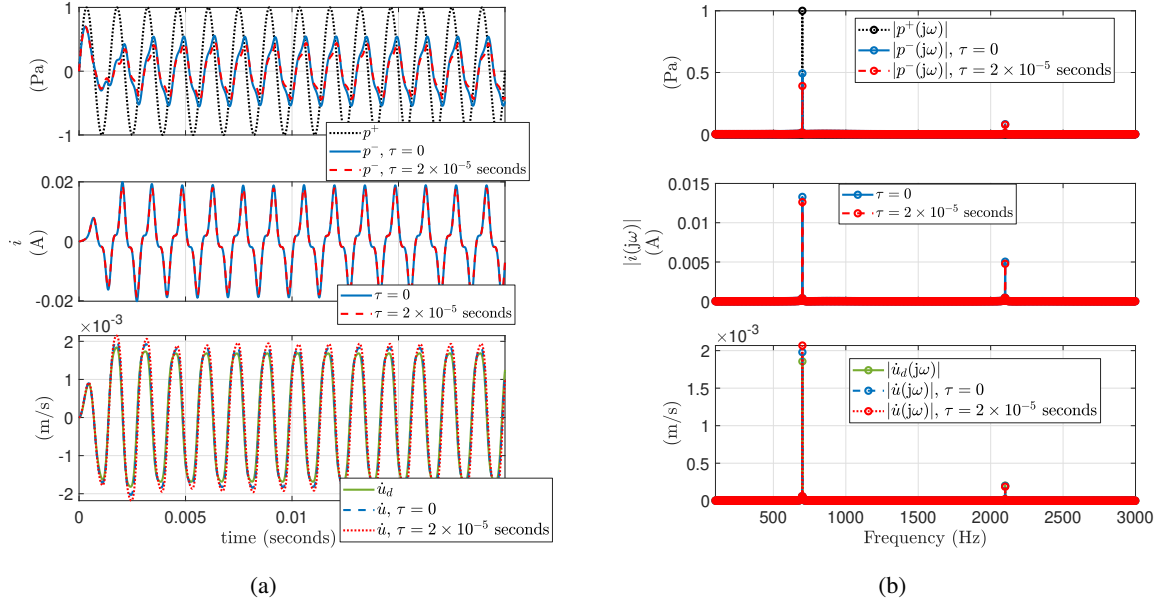


Figure 8: Time histories (a) and DFTs amplitudes (b) of incident p^+ and reflected p^- pressures, electrical current $i(t)$, target \dot{u}_d and actual \dot{u} velocities, in case of Duffing desired dynamics of the ER. The excitation p^+ is at 700 Hz. Both synchronous ($\tau = 0$) and delayed ($\tau = 2 \times 10^{-5}$ seconds) simulation results, are showed.

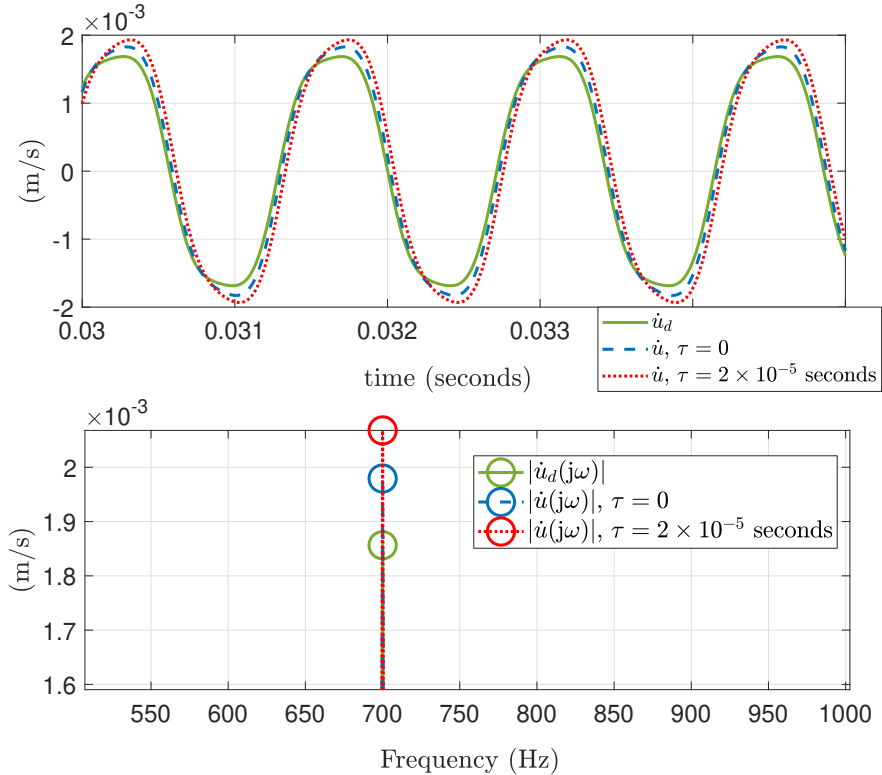


Figure 9: Time history zoom in the stationary regime (top) and DFTs amplitudes zoom at the fundamental harmonic 700 Hz (bottom), of target \dot{u}_d and actual \dot{u} velocities, in case of Duffing desired dynamics of the ER. Both synchronous ($\tau = 0$) and delayed ($\tau = 2 \times 10^{-5}$ seconds) simulation results, are showed.

Fig. 10 shows the spectra of the Fundamental and Third harmonics of the ER responses, in terms of the amplitudes of the target displacement $u_d(j\omega)$, of the actual displacement $u(j\omega)$ and of the electrical current $i(j\omega)$. The desired displacement fundamental-harmonic spectrum is compared to the Harmonic-Balance analytical solution at the first order (relative to a 1-term solution expansion, see Appendix B). The slight difference between the analytical solution and the numerical one is due to the errors in the numerical integration of Eq. (13). Notice the residual peak around f_0 in the plot of $|u(j\omega)|$ in Fig. 10. This is due to the difficulty to fully cancel out the ER open circuit dynamics. Such residual peak is present even in case of linear target dynamics, especially when $f_d \neq f_0$, as showed in [24], and its main cause is the time delay. In the zoomed area in Fig. 10, we spot a jump corresponding to the superharmonic resonance at about 3 times the primary nonlinear resonance frequency relative to the *fundamental* harmonics.

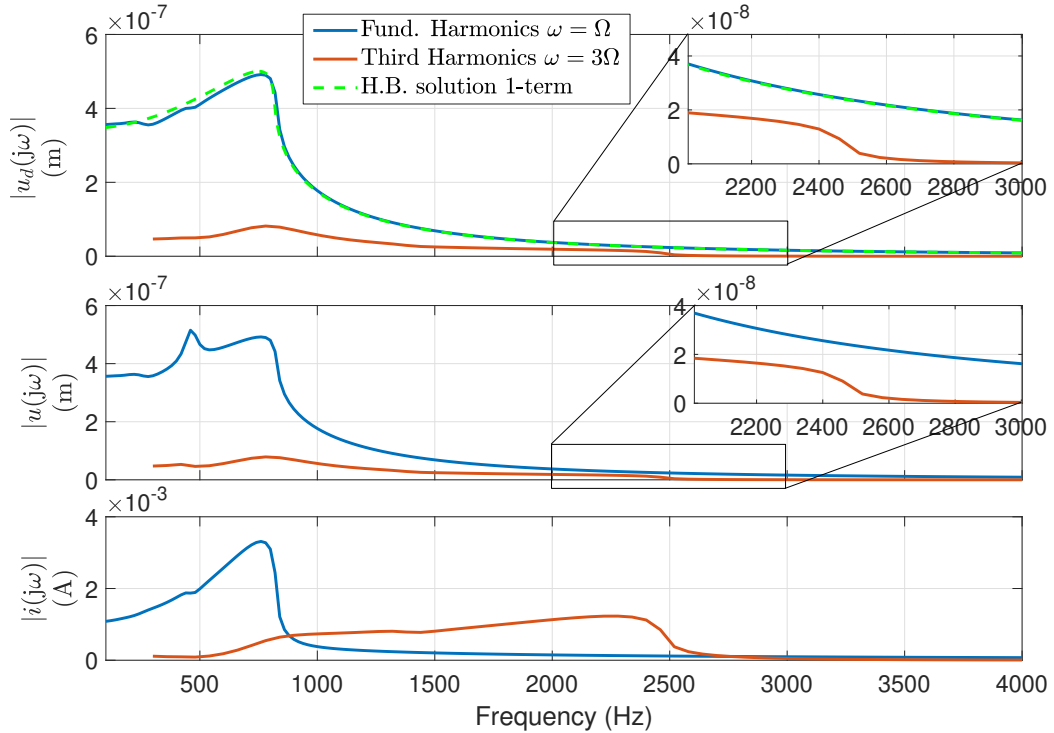


Figure 10: Fundamental and third Harmonics of the desired displacement amplitude $|u_d(j\omega)|$, and actual displacement amplitude $|u(j\omega)|$, in case of Duffing desired dynamics of the ER (with $\mu_M = \mu_K = 1$, $R_{at} = \rho_0 c_0$ and $\beta_{NL} = 1 \times 10^{13} \text{ m}^{-2}$). The target displacement fundamental harmonics are compared to the Harmonic-Balance 1-term analytical solution. The zoom of $|u_d(j\omega)|$ and $|u(j\omega)|$ is around the secondary jump.

Figs 11 and 12 show the fundamental harmonics of ER response, with varying target dynamics parameters or excitation amplitude. The ER response is given in terms of the ratio between electrical current and pressure amplitudes, as well as mobility (defined as $\dot{u}(j\Omega)/p(j\Omega)$) at the fundamental harmonics. Default values are $\mu_M = \mu_K = 1$, $R_{at} = \rho_0 c_0$, $\beta_{NL} = 1 \times 10^{13} \text{ m}^{-2}$ and $p_0^+ = 1 \text{ Pa}$. The huge value of the nonlinear coefficient β_{NL} is needed for the target dynamics to display its nonlinear behaviour at low excitation amplitudes. The higher β_{NL} is, the lower excitation levels are necessary to trigger the same nonlinear phenomena. Fig. 11a shows the effect of the variation of the nonlinear coefficient β_{NL} , while Fig. 11b shows the effect of varying the excitation amplitude p_0^+ . The typical “hardening spring” effect of Duffing-type oscillators with positive cubic nonlinearities [30], is evident and accentuated as higher the nonlinear coefficient or the excitation amplitude. The effect of varying the reactive and resistance terms in the ER desired dynamics, is illustrated in Fig. 12, showing that the jump moves toward higher frequencies for higher values of μ_K/μ_M , while a lower quality factor decreases the peak, hence smoothing the jump. These simulations demonstrate the tunability of the RTI control strategy also in case of a non-linear (Duffing) target dynamics achieved by the RTI algorithm exposed in Section 2.

Fig. 13 shows the responses in a *quasi-stationary* regime realized by a swept sine excitation of 5 seconds with

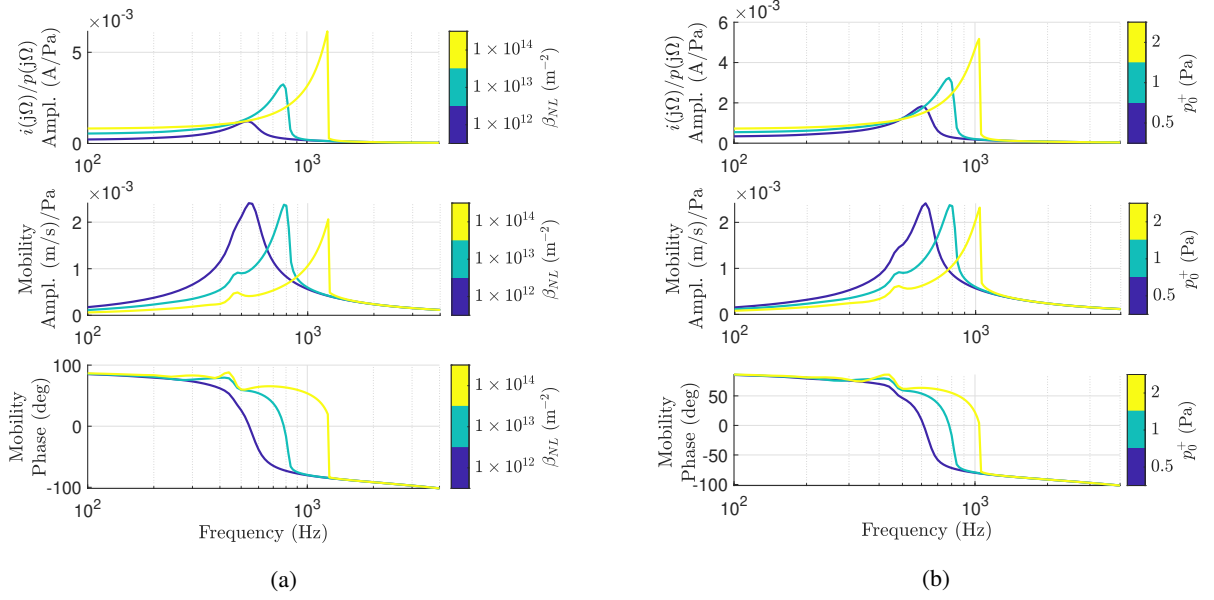


Figure 11: Amplitude of the fundamental harmonics of the simulated stationary responses of the ER to harmonic excitation p^+ , in terms of electrical current and acoustic mobility, in case of varying β_{NL} (a) and p_0^+ (b).

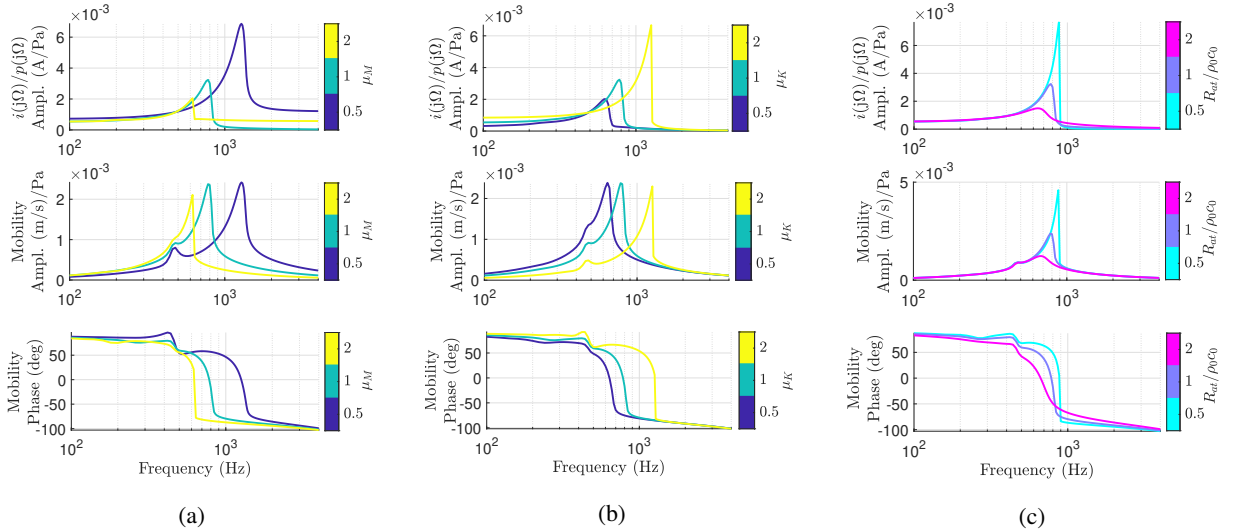


Figure 12: Amplitude of the fundamental harmonics of the simulated stationary responses of the ER to harmonic excitation p^+ , in terms of electrical current and acoustic mobility, in case of varying μ_M (a), μ_K (b) and R_{at} (c).

frequency varying between 300 and 1400 Hz in the *increasing* or *decreasing* sense. The target parameters are set to $\mu_M = \mu_K = 1$ and $R_{at} = \rho_0 c_0 / 4$. This simulation demonstrates another typical behaviour of nonlinear systems, i.e. the dependence upon the initial conditions. In particular, a cubic stiffness term realizes two possible stable responses in certain frequency ranges. Depending upon the frequency variation sense, the Duffing resonator initial response will be on the upper or the lower branch [30], jumping to the other stable response at higher or lower frequencies, respectively. In Fig. 13, the EA response is provided in terms of auto-power-spectral-densities (auto-PSDs) of desired velocity \dot{U}_d , electrical current I and actual velocity \dot{U} , divided by the auto-PSD of sound pressure P in front of the speaker diaphragm. The choice to present PSDs instead of pure FFTs, is firstly due to the non-stationary character of the

325
326
327
328
329
330
331
332

chirp excitation. Moreover, we divided the auto-PSDs by the sound pressure auto-PSD in order to retrieve analogous quantities of transfer functions, which are typically employed for linear responses, but which lose their significance in case of multi-harmonic field.

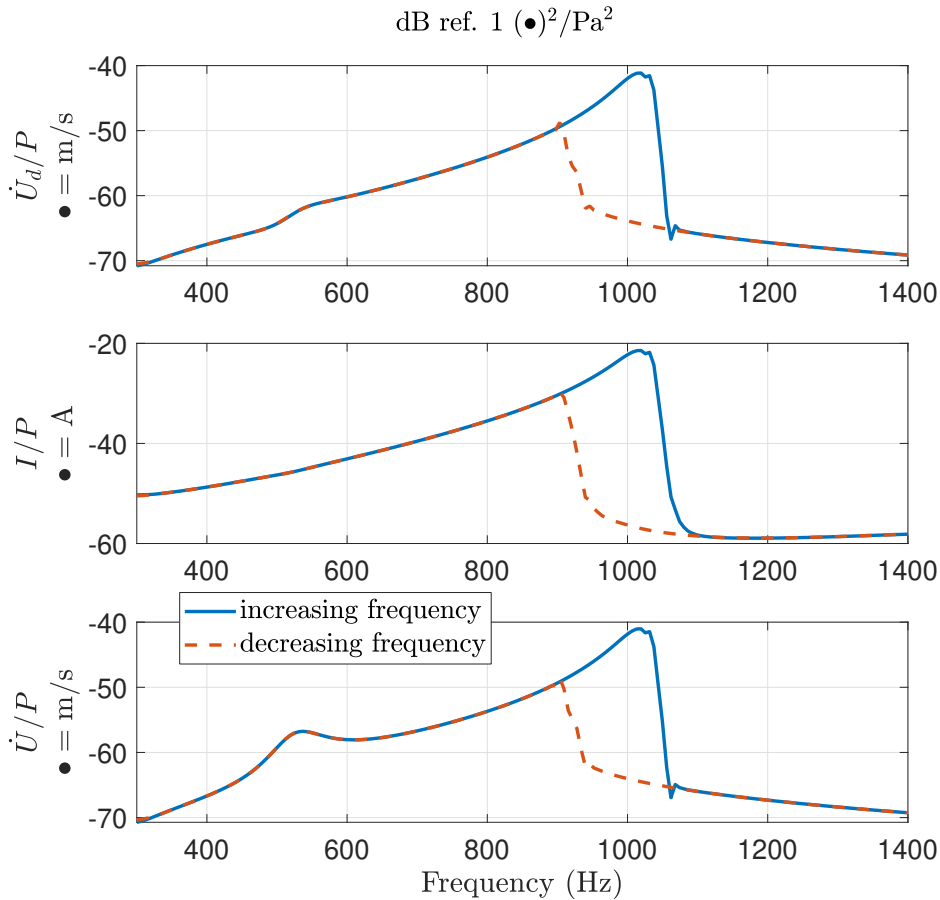


Figure 13: ER simulated responses in terms of auto-PSDs divided by sound pressure auto-PSD, in case of chirp excitation p^+ , with frequency increasing (solid blue) and decreasing (dashed red) between 300 and 1400 Hz.

4. Experimental validation

In this Section, the RTI algorithm is experimentally implemented to target a linear (in Section 4.1) and a nonlinear dynamics (in Section 4.2) of the ER. Signal acquisition and control implementation are operated by a D-Space MicroLabBox DS1202 hardware. The system is described in Fig. 14: the pressure p on the speaker diaphragm, estimated by four microphones around the membrane, after being digitally converted by the Analogue-Digital-Converter (ADC), is fed into a *programmable* digital signal processor (DSP) where the output of the control is computed at each time step. The Howland current pump [31] allows to enforce the electrical current i in the speaker coil independently of the voltage at the loudspeaker terminals. It consists of an operational amplifier, two input resistors R_i , two feedback resistors R_f , and a current sense resistor R_s . The resistance R_d and capacitance C_f constitutes the compensation circuit to ensure stability with the grounded load [32].

The ER prototype employed for the experimental validation is photographed in Fig. 15a. It consists of a central speaker with four corner microphones used to retrieve the averaged pressure on the speaker. The back-case accommodates the analogical electronic card interfacing with the D-Space. The test-bench to measure pressure and velocity on the speaker diaphragm is illustrated in Fig. 15b. An external acoustic source excites the ER, whose dynamics

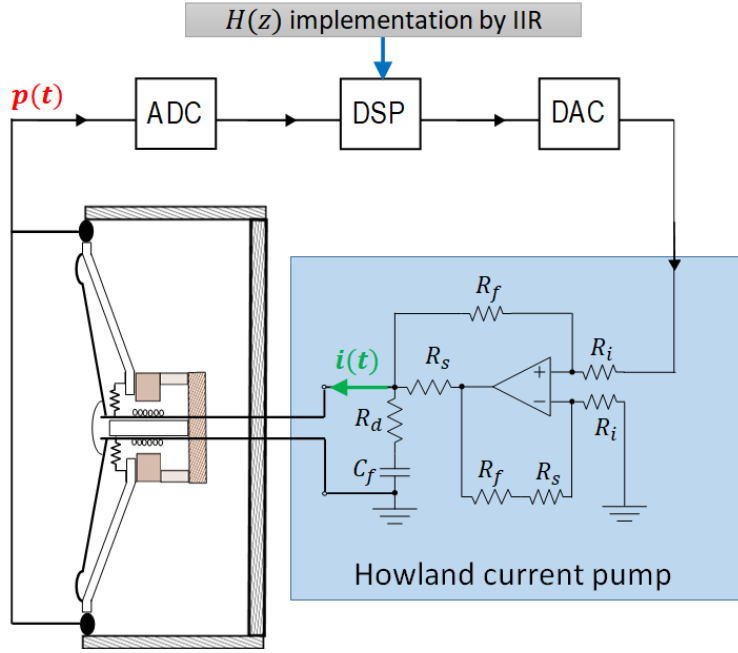


Figure 14: Sketch of the ER architecture.

Thiele-Small parameters	M_{a0}	R_{a0}	K_{a0}	Bl/S_d
Units	$\text{kg}\cdot\text{m}^{-2}$	$\text{Pa}\cdot\text{s}\cdot\text{m}^{-1}$	$\text{Pa}\cdot\text{m}^{-1}$	$\text{Pa}\cdot\text{A}^{-1}$
Values	0.392	194	4.25×10^6	191

Table 1

Thiele-Small parameters of the ER.

is retrieved in terms of sound pressure (by an external Brüel and Kjaer microphone) and normal velocity at the centre of the speaker diaphragm (by a Laser-Doppler-Velocimeter LDV). The noise source is placed on a caoutchouc basis in order to isolate it from the heavy mass basis, where the rest of the equipment is placed. Fig. 16 is a sketch of the entire experimental setup. It comprises the ER system with its power supply and digital communication with the DSPACE, the external microphone and LDV, and the external noise source (a loudspeaker). The DSPACE communicates with a computer where the digital control is defined and where the measurements data can be retrieved (through the Simulink toolbox of Matlab). The channels of the DSPACE have been differentiated between those concerning the control algorithm (C.I. and C.O. for control-input and control-output), and those employed for measuring the performance (M.I. and M.O. for measurement-inputs and measurement-output).

The acoustic environment cannot be rigorously defined as *open-field*, nevertheless the coupling with the acoustic modes of the (large) room where the test is carried out, is sufficiently weak to be able to retrieve the response of an acoustic Duffing resonator alone, with low influence of the acoustic environment.

The parameters of the loudspeaker SDOF model employed for the model-inversion algorithm, are reported in Table 1. They have been estimated by impedance measurements in different configurations, as reported in [29].

4.1. The Linear target dynamics

As already done numerically, we prove, also experimentally, the equivalence of the RTI and classical IIR convolution algorithms to target LTI mechano-acoustical dynamics. In order to check the reliability of the RTI control strategy in following the linear target dynamics of Eq. (14) in a transient evolution, a first test has been conducted by triggering an external sound source, emitting a pure sine at 500 Hz, after 3 seconds. Fig. 17 shows the time histories of pressure, electrical current $i(t)$ and target and measured velocities (\dot{u}_d and $\dot{u}(t)$ respectively) on the speaker diaphragm. The target SDOF parameters are chosen as $\mu_M = \mu_K = 1$ and $R_{at} = \rho_0 c_0$. The results obtained by the IIR

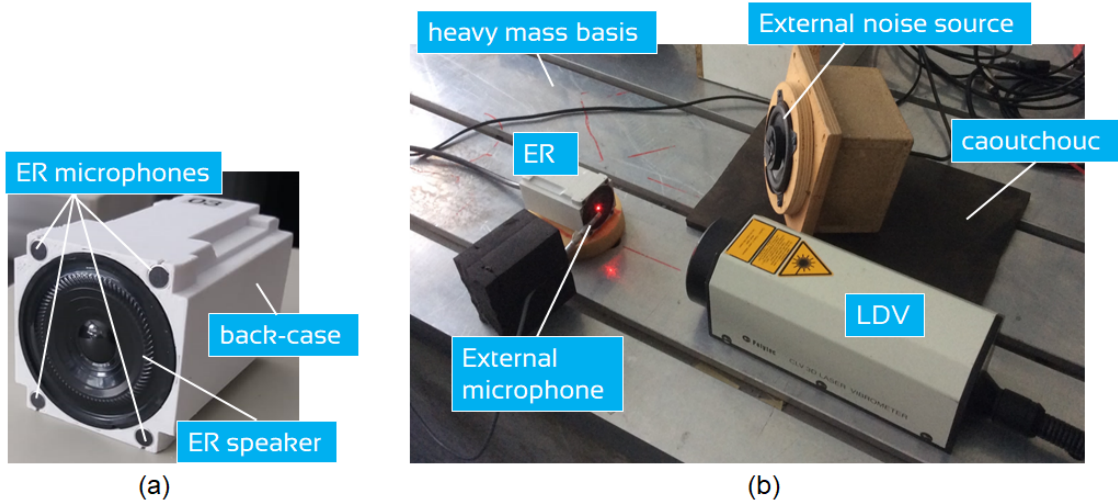


Figure 15: Photos of the ER prototype (a) and of the experimental test-rig (b) for the measurement of pressure and velocity on the speaker diaphragm.

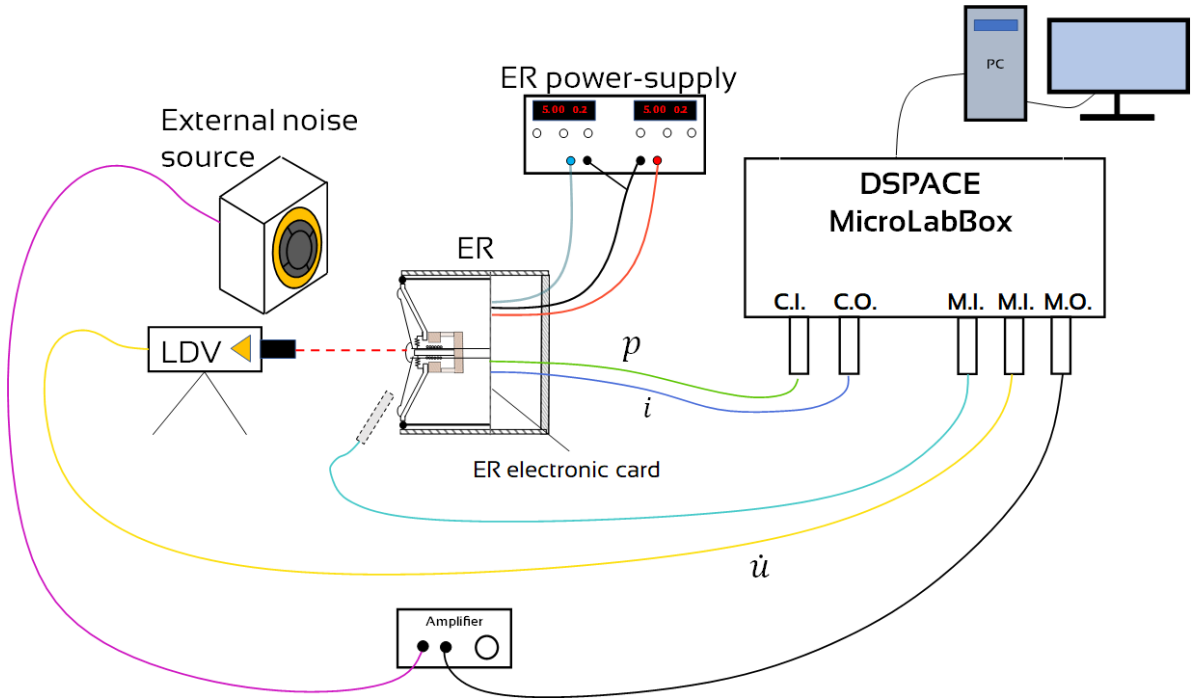


Figure 16: Sketch of the entire experimental setup.

implementation are reported in Fig. 17a, while the RTI outcomes are given in Fig. 17b. Notice how the RTI technique allows to immediately follow the target velocity in the same way as the classical IIR. The dephasing between \dot{u}_d and $\dot{u}(t)$ mostly depends upon the inevitable time delay in the digital control implementation of the controller [24], which seems to be unaffected by the control algorithm employed (it looks the same in both IIR and RTI), other than the model-uncertainties in the control synthesis.

In Fig. 18a, the normalized mobility transfer function is plotted in amplitude and phase, along with the coherence for $\mu_M = \mu_K = 1$ and $R_{at} = \rho_0 c_0$ in the frequency range 100-3000 Hz, for both IIR and RTI techniques. The mobility

371
372
373
374
375
376
377

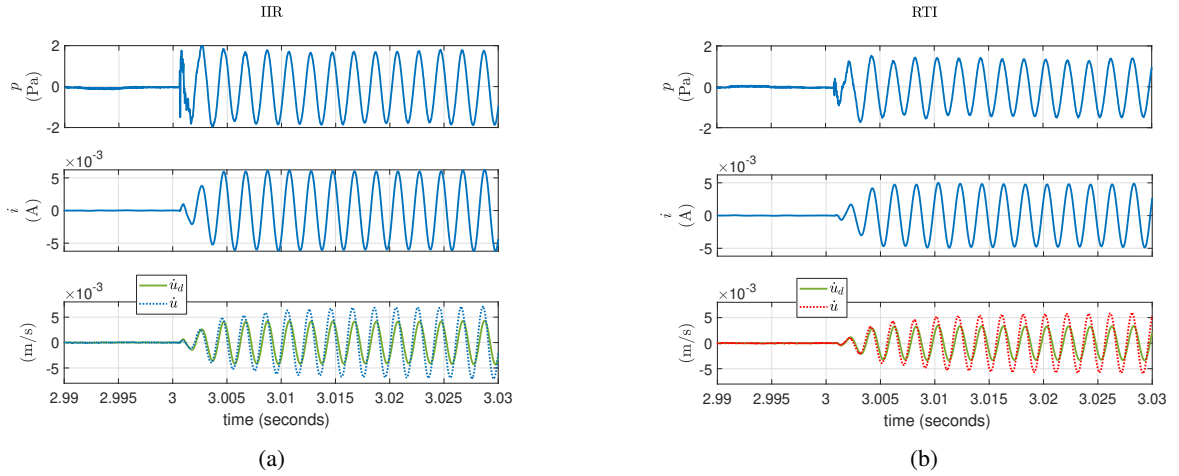


Figure 17: Time histories of pressure $p(t)$, electrical current $i(t)$ and desired and measured velocities (\dot{u}_d and $\dot{u}(t)$ respectively) on the speaker diaphragm, when an external sound source emitting a pure sine at 500 Hz, is activated after $t = 3$ seconds. A linear SDOF dynamics of the ER with $\mu_M = \mu_K = 1$ and $R_{at} = \rho_0 c_0$ is targeted either by the IIR **(a)** or by the RTI **(b)** implementation strategy.

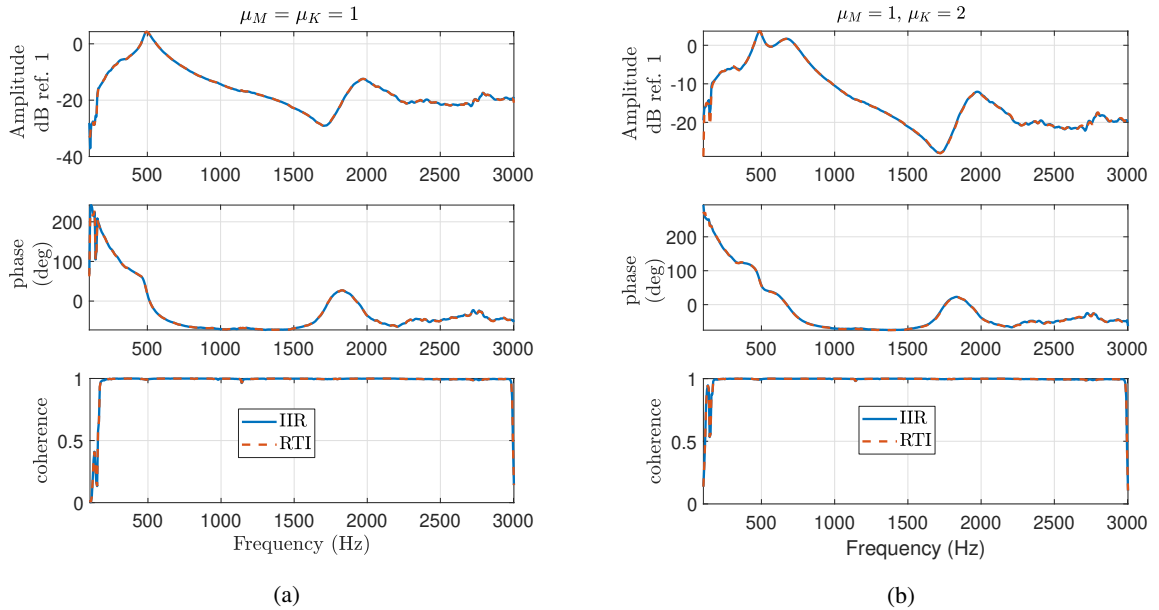


Figure 18: Mobility **(b)** obtained by targeting a linear SDOF dynamics of the ER with $\mu_M = \mu_K = 1$ and $R_{at} = \rho_0 c_0$ **(a)** and $\mu_M = 1$, $\mu_K = 2$ and $R_{at} = \rho_0 c_0$ **(b)** by either the IIR (solid blue line) or the RTI (dashed red line).

is also plotted in case of $\mu_M = 1$, $\mu_K = 2$ and $R_{at} = \rho_0 c_0$ in Fig. 18b. Observe in Fig. 18b that both the IIR and RTI algorithms are equally incapable to fully cancel out the original speaker dynamics at f_0 , mainly because of time delay [24]. Hence, a residual peak is present around f_0 Hz. The loudspeaker mode employed for the model inversion is the one around f_0 , while an additional loudspeaker mode (not taken into account in the model inversion) appears around 2000 Hz. Fig. 19a shows the auto-PSDs of desired $\dot{U}_d(\omega)$ and actual $\dot{U}(\omega)$ velocity in case of $\mu_M = \mu_K = 1$ and $R_{at} = \rho_0 c_0$, while Fig. 19b shows the corresponding percentage error, for both the IIR and RTI control strategies. The percentage error on the velocity auto-PSD is defined as:

378
379
380
381
382
383
384

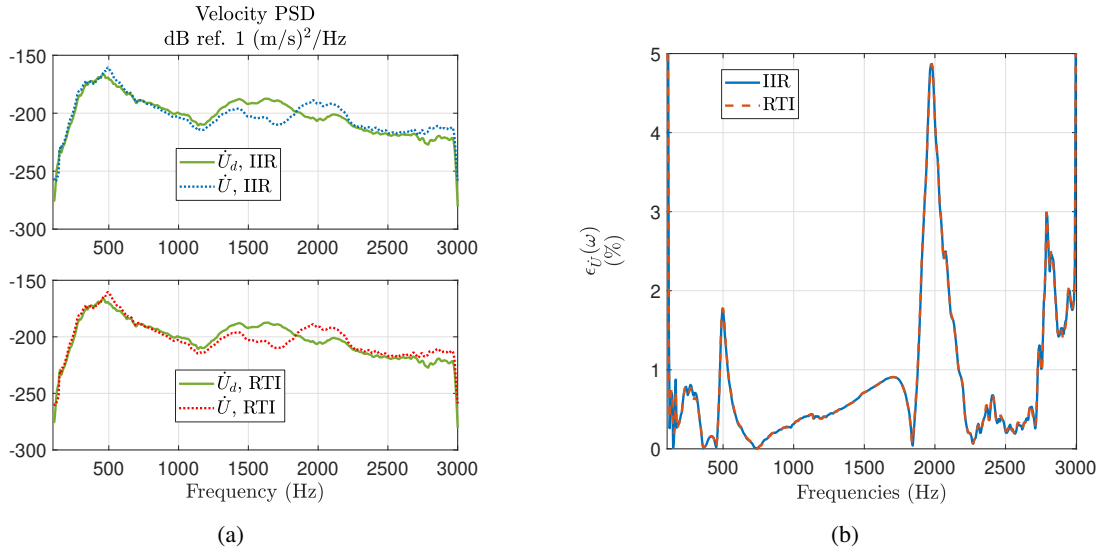


Figure 19: Auto-PSDs of desired \dot{U}_d and actual \dot{U} velocity **(a)**, and corresponding error percentage **(b)**, obtained by targeting a linear SDOF dynamics of the ER with $\mu_M = \mu_K = 1$ and $R_{at} = \rho_0 c_0$ by either the IIR or the RTI.

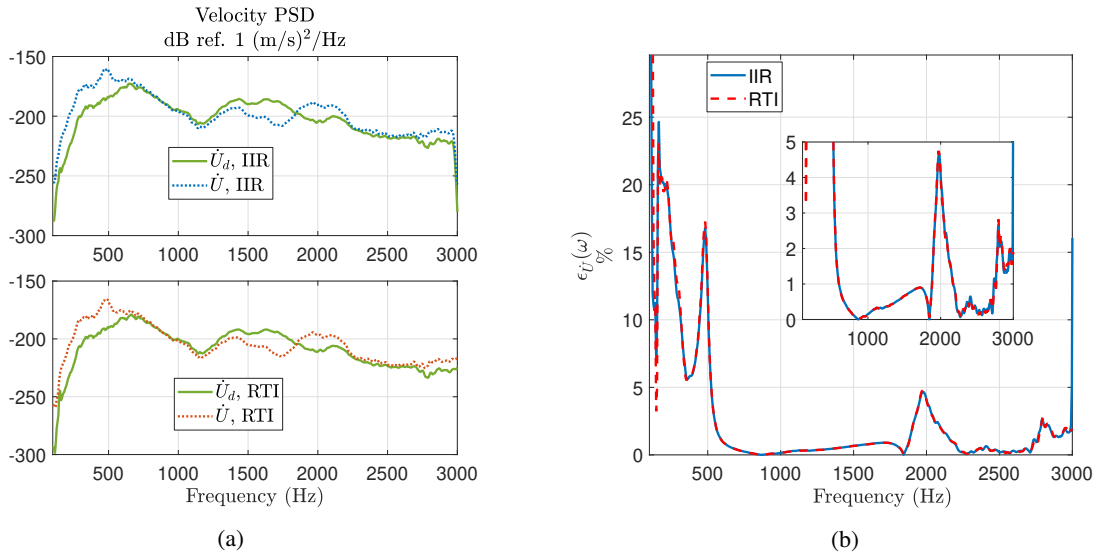


Figure 20: Auto-PSDs of desired \dot{U}_d and actual \dot{U} velocity **(a)**, and corresponding error percentage **(b)**, obtained by targeting a linear SDOF dynamics of the ER with $\mu_M = 1$, $\mu_K = 2$ and $R_{at} = \rho_0 c_0$ by either the IIR or the RTI.

$$\epsilon_{\dot{U}}(\omega) = \frac{|\dot{U}(\omega) - \dot{U}_d(\omega)|}{\dot{U}_d(\omega)}. \quad (16)$$

Observe that the spectrum of $\epsilon_{\dot{U}}(\omega)$ is exactly the same for both the RTI and the IIR control algorithms, as expected 385
 by the mobility plots of Fig. 18. Apart from the low-frequency region of weak coherence (check Fig. 18), the percentage 386
 error stays below 1% at all frequencies except around the speaker own resonance of the controlled mode (500 Hz) and 387
 around the additional uncontrolled mode of the speaker (nearly 2000 Hz). The cause of the IIR lost of performance 388
 at the speaker own resonance is due to the physiological time delay of the digital control system, as it has been 389
 demonstrated in [24]. The error around 2000 Hz is due to the presence of an additional mode of the speaker which has 390

not been taken into account in the model-inversion control. In Fig. 20a, it is showed the velocity auto-PSD reached by both IIR and RTI, for target parameters $\mu_M = 1$ and $\mu_K = 2$, which means a target frequency $f_d = \sqrt{2}f_0 \approx 740$ Hz. Moving f_d away from f_0 , causes an increase in the residual pick around the original resonance frequency, and consequently a higher percentage error (about 17%) around f_0 , as showed in Fig. 20b. Such error which, as commented above, is due to the residual speaker dynamics when $f_d \neq f_0$, will appear also in case of Duffing-like target dynamics, as it also entails a shift of the resonance frequency because of nonlinearity. The percentage error $\epsilon_{\dot{U}}$ falls below 1% soon after f_0 , and reaches about 5% at 2000 Hz because of the additional speaker mode. We highlight here that the RTI control algorithm we propose in this contribution, demonstrates to not add any additional error in its experimental implementation for linear target dynamics with respect to widely employed IIR control algorithms. Recent works have demonstrated that a control exploiting also a microphone inside the back-cavity of the ER, is able to increase the robustness of the control and significantly reduce the residual pick at f_0 for linear target dynamics [33].

In Appendix A, the target parameters of Eq. 14 are modified in order to assess the equivalence between the IIR and the RTI approaches in tuning the linear target dynamics parameters.

Once assessed the reliability of the RTI algorithm in the linear case, as equivalent to the classically accepted IIR strategy, let us now verify, experimentally, its potential to enforce nonlinear mechano-acoustical dynamics on the ER.

4.2. The Duffing-type target dynamics

As in the numerical simulations, here we experimentally target the Duffing-type mechano-acoustical dynamics of Eq. (15). As for the linear case, the performance of the RTI is first proved in the transient regime. Hence, an external sound source emitting a pure sine at 700 Hz is triggered after 3 seconds, and the response of the ER is reported in terms of measured pressure, current and velocity in Fig. 21. Fig. 22a displays a zoom in the stationary regime of the time signals. The electrical current clearly shows the presence of higher harmonics, which bring about the multi-harmonic response of the ER diaphragm as it appears in the plot of the measured $\dot{u}(t)$. Fig. 22b shows the Fast-Fourier-Transform (FFT) of the time signals. The system responds with a secondary resonance (related to the free oscillations) at 3 times the excitation frequency as common of Duffing resonators. Observe how the measured velocity \dot{u} detaches from the target one \dot{u}_d in exactly the same way as in the simulations of Fig. 9, when a time delay τ was simulated in the algorithm. For the reader to visualize the importance of time delay in the response of our ER with a Duffing-like target dynamics, we report, in Fig. 23, the comparison between simulated and measured velocity. Notice how the experimental signal follows the simulated trend, apart from some measurement noise and physiological differences due to the uncertainties of the speaker model employed in the simulations. As for LTI target behaviour [24], time delay is the main responsible for the errors also when targeting Duffing-like dynamics.

In Fig. 24 the auto-PSDs of pressure (P) on the speaker diaphragm, of electrical current (I) and of velocity (\dot{U}) are plotted, comparing the Open-Circuit (O.C.) performance to the cases of control with linear or Duffing target dynamics. The auto-PSDs are retrieved from a swept sine excitation with frequency increasing between 100 and 3000 Hz in 10 seconds. The ‘‘jump’’ phenomenon due to the cubic function of $u(t)$ in the restoring force of the spring, typical of the Duffing resonator, clearly appears at about 890 Hz. Observe also that the dynamics at the original (open-circuit) resonance of the ER (around 500 Hz) is not totally cancelled out by the model-inversion control, in case of Linear as well as Duffing-like target dynamics. Notice that the pressure auto-PSDs in Fig. 24 are almost the same for each configuration, demonstrating that the nonlinear behaviour is achieved thanks to the control and is not naturally triggered in the speaker by high excitation levels. The target SDOF resonator parameters are $M_{at} = M_{a0}$, $K_{at} = K_{a0}$ and $R_{at} = \rho_0 c_0$, while the cubic term in the Duffing case is multiplied by a $\beta_{NL} = 1 \times 10^{13} \text{ m}^{-2}$. Notice also the jump phenomenon of the superharmonic resonance at about 2670 Hz, which is exactly 3 times the primary nonlinear resonance frequency relative to the *fundamental* harmonics. This is the so-called *superharmonic resonance* [30] already found in the numerical simulations (see Fig. 10), which is evident in the electrical current plot, and slightly in the velocity spectrum. Observe that the velocity on the speaker diaphragm is also affected by the afore-mentioned additional loudspeaker mode at about 2000 Hz.

Fig. 25a shows the auto-PSDs of desired \dot{U}_d and actual \dot{U} velocity in case of $\mu_M = \mu_K = 1$, $R_{at} = \rho_0 c_0$ and $\beta_{NL} = 1 \times 10^{13} \text{ m}^{-2}$, with the corresponding error $\epsilon_{\dot{U}}$ plotted in Fig. 25b. As mentioned in Section 4.1, the shift of the target resonance entails a high error around the open-circuit mode f_0 , with the error increasing as more the target resonance is shifted away from f_0 . Here, due to the nonlinearity, the resonance is moved above 900 Hz, and the percentage error reaches almost 30%. However, the jump is perfectly followed by the actual velocity spectrum, and the error stays below 1% from 670 to 1900 Hz.

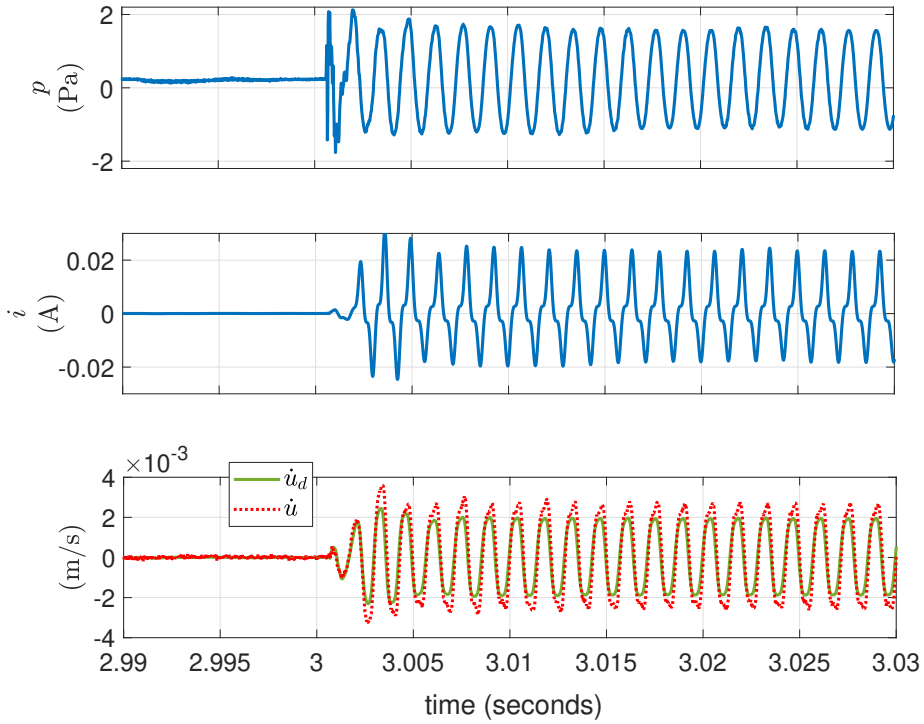


Figure 21: Time histories of pressure $p(t)$, electrical current $i(t)$, target and measured velocities (\dot{u}_d and $\dot{u}(t)$) respectively on the speaker diaphragm. An external sound source emitting a pure sine at 700 Hz, is activated after $t = 3$ seconds. The linear target SDOF dynamics of the ER has $\mu_M = \mu_K = 1$, $R_{at} = \rho_0 c_0$ and $\beta_{NL} = 1 \times 10^{13} \text{ m}^{-2}$.

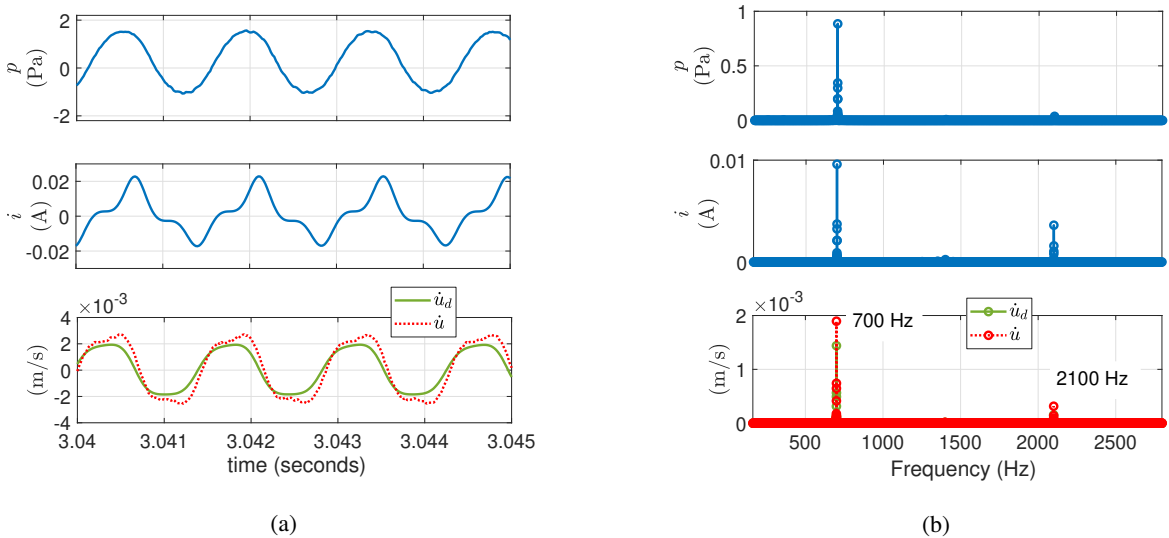


Figure 22: Zoom (a) of Fig. 21 in the stationary regime, and its DFT (b).

In the following, either the target dynamics parameters or the excitation amplitude have been varied in order to identify typical Duffing-resonator responses and experimentally validate the tunability of such nonlinear system. The

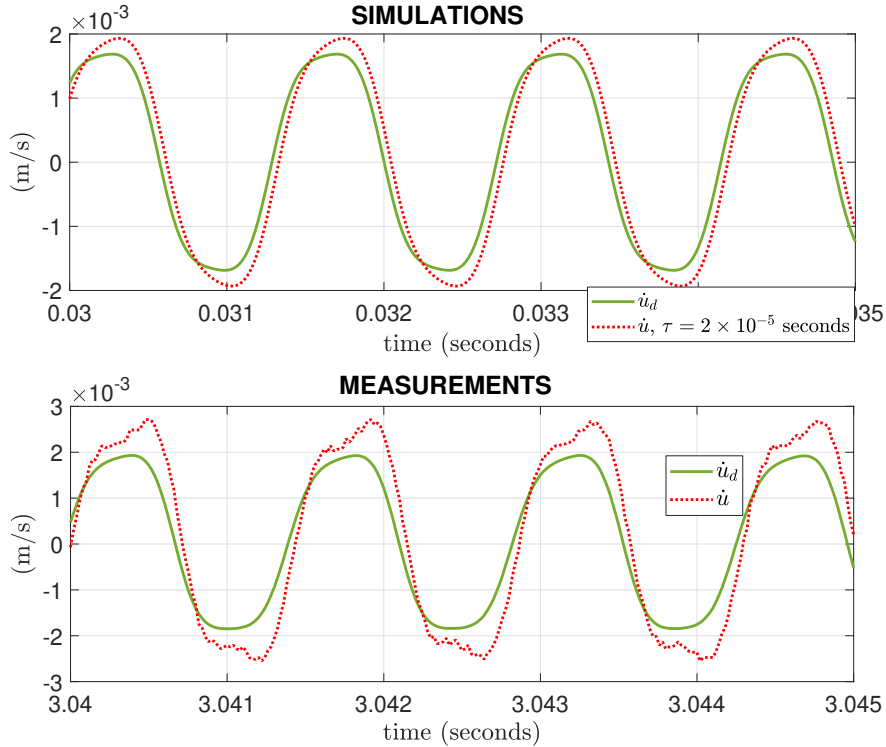


Figure 23: Simulated (top) and measured (bottom) time histories of desired (solid green) and actual (dotted red) velocities on the speaker diaphragm excited by an external sound source emitting a pure sine at 700 Hz. The simulated response considers a time delay in the control of $\tau = 2 \times 10^{-5}$. The linear target SDOF dynamics of the ER has $\mu_M = \mu_K = 1$, $R_{at} = \rho_0 c_0$ and $\beta_{NL} = 1 \times 10^{13} \text{ m}^{-2}$.

ER responses are presented in terms of auto-PSDs of target velocity, electrical current and actual velocity, divided by the auto-PSD of sound pressure. The reason for that choice is that the transfer functions typically employed to characterize linear responses, lose their significance in case of multi-harmonic field. The PSDs ratio provides a form of function which is the closest to the transfer function, allowing us to compare the experimental trends to the numerical ones. Nevertheless, the PSDs ratio does not distinguish between fundamental and higher harmonics, as it was possible in numerical simulations. To separate incident and scattered fields and retrieve the fundamental and higher harmonics separately, a dedicated experimental setup should be conceived, which will be the subject of another contribution of this article series, where both *acoustical passivity* (in the sense given by [24]) and *absorptive performance* of this Duffing-like resonator will be investigated. Indeed, the experimental test-rig employed in this work, does not allow to separate the incident field from the multi-harmonic scattered field. Moreover, the *fundamental* harmonic waves are not physically uncoupled by the *non-fundamental* ones as the acoustic environment of the test-bench is non-perfectly *open*, hence a multi-harmonic scattered field entails also a multi-harmonic excitation field. Nevertheless, even supposing to achieve perfect anechoicity around the experimental setup, the LDV closely facing the ER, as well as the sound source itself, might introduce a field scattered back to the ER speaker. The problem of separation of incident and scattered fields in nonlinear acoustic absorbers requires non-trivial strategies to solve the multi-harmonic scattering problem, as presented in [34, 35] for example.

As done in the numerical simulations, we plot the dependency of the frequency response upon the excitation amplitude in Fig. 26b. Since, as said before, it was not possible to separate experimentally the incident from the scattered fields, we refer in Fig. 26b to the variation of the external acoustic source signal (the voltage at the external loudspeaker terminals), and not to the variation of the incident pressure field amplitude p_0^+ (as in the numerical simulations of Fig. 11b). This is also the reason for which a direct superposition between numerical simulations and measurements is not possible, as we miss the information about the incident pressure field corresponding to the external source signal.

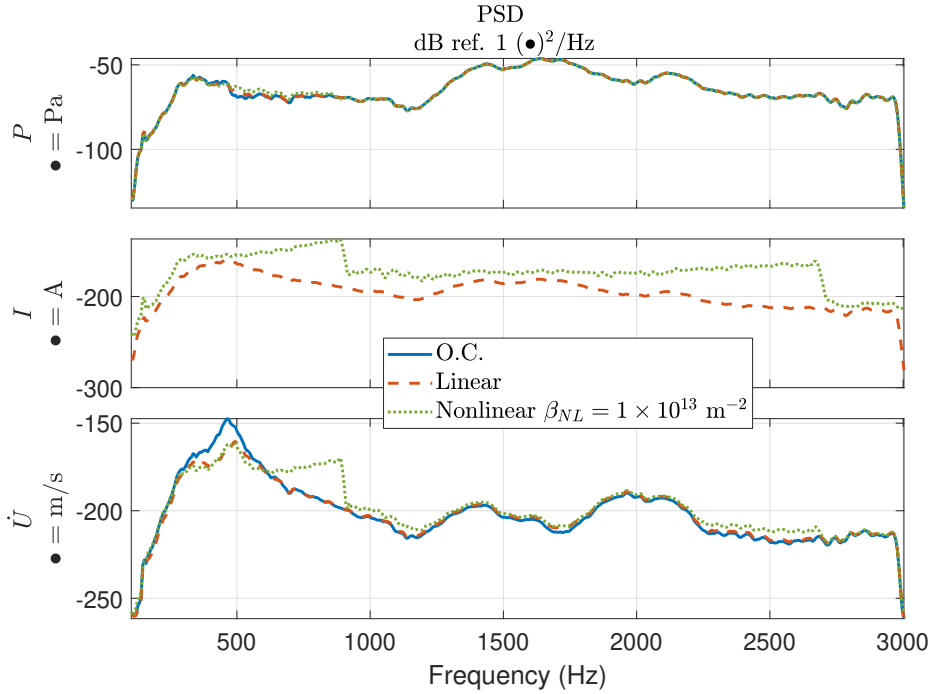


Figure 24: Auto-PSDs of pressure, electrical current and velocity between 100 and 3000 Hz, in case of open circuit (O.C.) loudspeaker (solid blue), Linear with $\mu_M = \mu_K = 1$ and $R_{at} = \rho_0 c_0$ (dashed red) and Duffing with $\beta_{NL} = 1 \times 10^{13} \text{ m}^{-2}$ (dotted green) target dynamics.

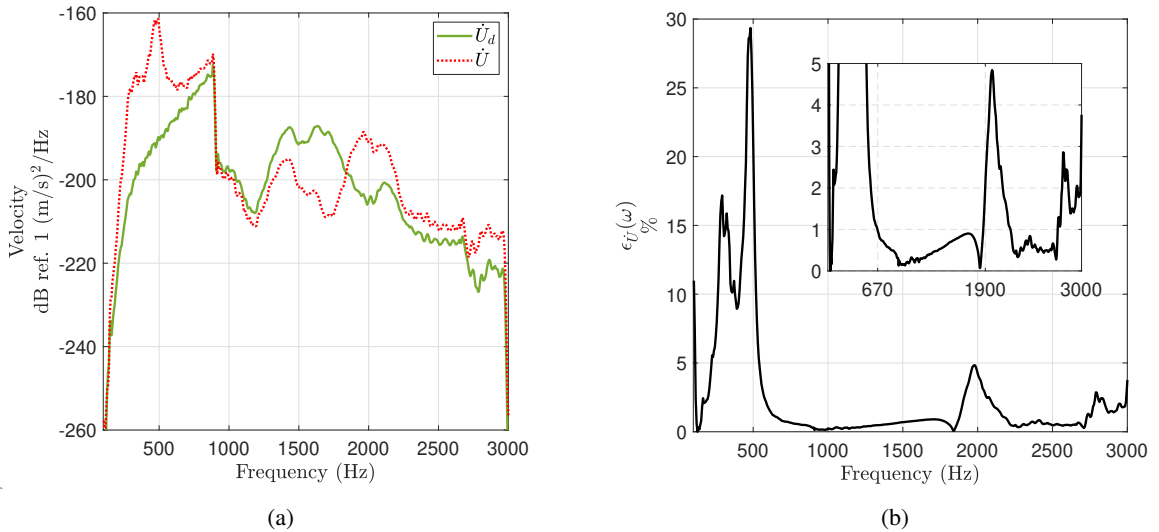


Figure 25: In (a), the auto-PSDs of the target \dot{U}_d and measured \dot{U} velocity, in case of $\mu_M = \mu_K = 1$ and $R_{at} = \rho_0 c_0$. In (b), the corresponding percentage error spectrum.

Nonetheless, by halving and doubling the external source signal, we can verify the trends showed in Fig. 11b. As the excitation increases, the resonance frequency moves toward higher frequencies and the jump sharpens, as expected. As in simulations, the effect of increasing the external excitation is similar to the one of augmenting β_{NL} , the latter

467
468
469

being showed in Fig. 26a. Notice how in case of $\beta_{NL} = 1 \times 10^{14} \text{ m}^{-2}$, the resonance moves toward 2000 Hz, where another speaker mode resonates, affecting the spectrum shape of the ER responses. 470
471

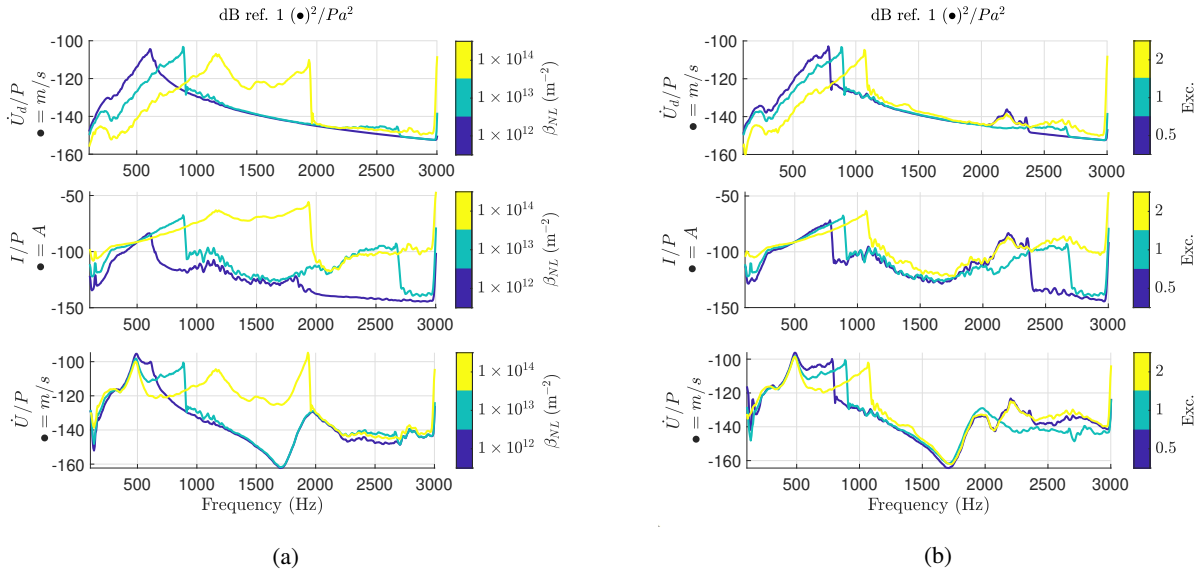


Figure 26: Auto-PSDs of target velocity, electrical current and actual velocity, divided by the auto-PSD of pressure, for varying β_{NL} (a) and excitation amplitude (b).

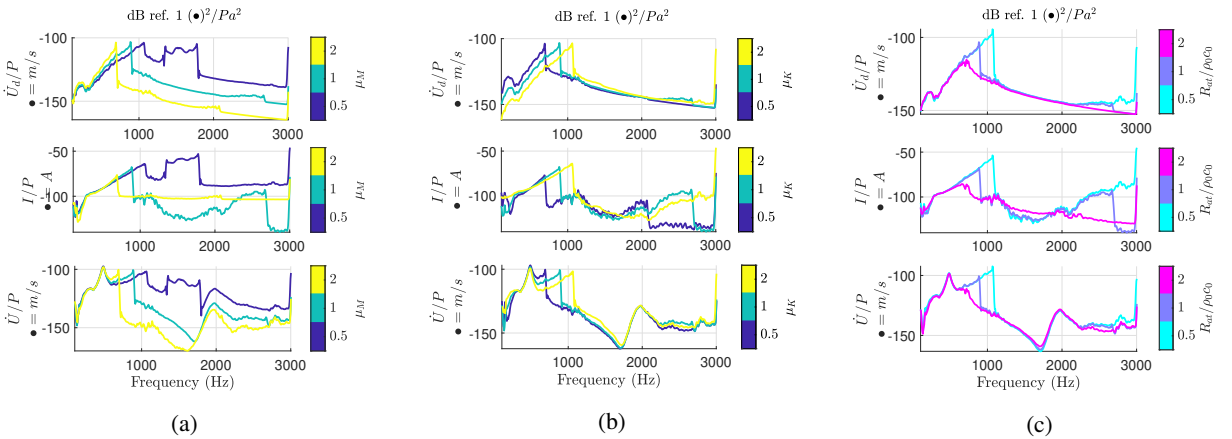


Figure 27: auto-PSDs of target velocity, electrical current and actual velocity, divided by the auto-PSD of pressure, for varying μ_M (a), μ_K (b) and R_{at} (c).

In the following figures, we demonstrate the ability to tune each of the term in the target Duffing resonator dynamics, by our RTI control. Fig. 27 experimentally proves the tunability of the Duffing dynamics by varying the target mass, linear stiffness and resistance terms. Apart from the expected behaviours in accordance with the simulations, some unexpected resonances occur in case of $\mu_M = 0.5$. Observe that, in case of linear desired dynamics and IIR algorithm, a lower target mass has been associated with lower level of acoustical passivity [24] after the target resonance, due to time delay. The effect of combining non-passive behaviours of fundamental harmonics on the one hand, with the higher harmonics produced by the nonlinearity on the other, is hard to predict at the present moment, but is likely to be behind these unexpected jumps at 1355 and 1776 Hz. Indeed, these unpredicted trends are present only in case of the lowest value of μ_M , suggesting the involvement of acoustical non-passivity. Proper formulations of 472
473
474
475
476
477
478
479
480

both acoustical passivity and absorptive performances for nonlinear resonators, could be tackled when the full multi-harmonic scattering problem will be solved by ad-hoc test-rigs as the ones presented in [34, 35]. Finally, in Fig. 28 we experimentally verify the double-branch solution of Duffing-like resonators, as done numerically in Fig. 13. Fig. 28 shows the responses in a *quasi-stationary* regime realized by a chirp excitation of 30 seconds with frequency varying between 100 and 3000 Hz in the *increasing* or *decreasing* sense. As expected, by varying the frequency in decreasing sense, both the fundamental and secondary jumps shift toward lower frequencies.

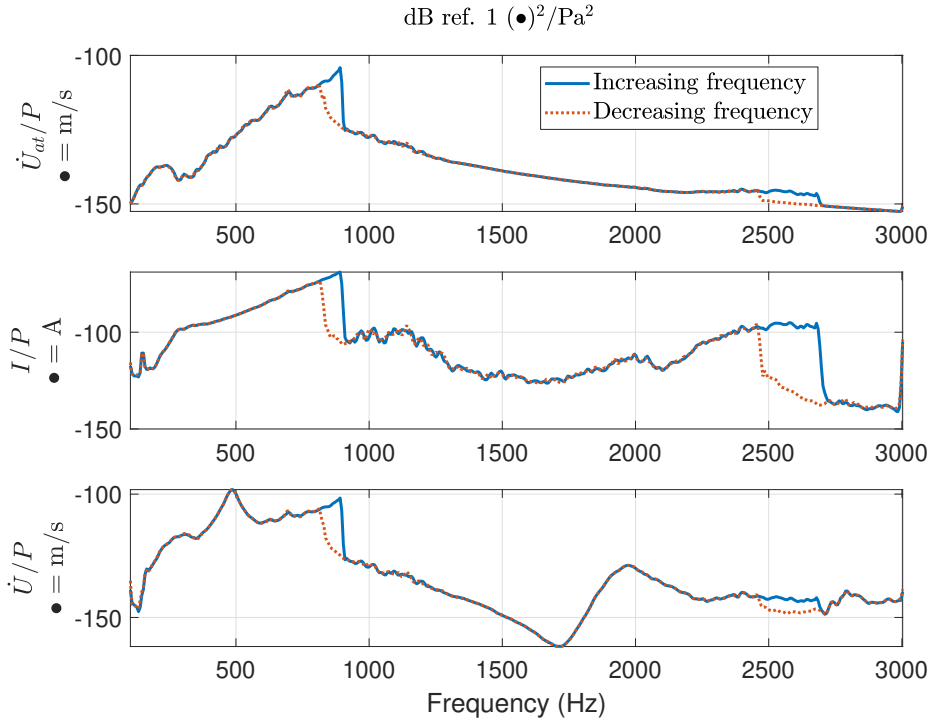


Figure 28: PSDs of target velocity, electrical current and actual velocity, divided by the PSD of pressure, for *forward* or *backward* linear variation of frequency in the chirp excitation. The terms of the target dynamics are fixed as $\mu_M = \mu_K = 1$, $R_{at} = \rho_0 c_0$ and $\beta_{NL} = 1 \times 10^{13} \text{ m}^{-2}$.

Figs 26, 27 and 28, demonstrate that the RTI algorithm for the first time exposed in this contribution, is capable to reproduce a tunable Duffing-like behaviour of the ER at low excitation levels, without the need of additional displacement sensors.

5. Conclusions

This paper has proposed the enlargement of the model-inversion technique to control the impedance of an Electroacoustic Resonator, toward non-*Linear-Time-Invariant* target dynamics, based upon the sole measurement of the pressure on the speaker diaphragm. As the measurement of the electroacoustic resonator diaphragm displacement $u(t)$ was not available, a Duffing-type response could not be achieved by simply inserting the cubic power of $u(t)$ in the controller (as proposed in [21]), and an alternative strategy had to be devised. Via representation of the model-inversion control in the state-space, and by interpreting the state-vector of the controller as the state-vector of the target dynamics, we have proposed an alternative algorithm capable of targeting *Linear-Time-Invariant* as well as non-*Linear-Time-Invariant* responses. Clearly, the possibility to exploit a measurement of the motion of the speaker (such as by a microphone in the back cavity as in [21] and [33]) in our Real-Time-Integration control scheme, might allow to reduce the problems of residual original dynamics. Nevertheless, compared to [21], which still relies on an Infinite-Impulse-Response convolution scheme, our Real-Time-Integration control strategy has already demonstrated significantly higher tunability (a large range of resonator parameters have been spanned) and performances, despite

not disposing of the additional displacement feedback.

In order to validate our Real-Time-Integration control strategy, it has been tested first for linear target dynamics, demonstrating its equivalence with respect to classical convolution-based correctors. Then, it has been tested against target Duffing-type dynamics with hardening behaviour. In order to retrieve the response of the nonlinear system uncoupled from external acoustic modes, the control algorithm has been simulated in an open-field external acoustic environment, by solving the *non-ideal* problem, such it is the open-field response of the Electroacoustic Resonator, where the sound pressure cannot be considered as a known term. After the numerical validation, our control has been experimentally tested on a prototype of electroacoustic resonator, in a quasi-open field acoustic environment, reproducing the expected trends and demonstrating the tunability of the control in varying all parameters of the Duffing target response. Since in case of linear target dynamics the Real-Time-Integration algorithm is totally equivalent to the Infinite-Impulse-Response, the former can be considered as a natural extension of the latter, opening up the model-inversion concept to nonlinear target dynamics. Some unexpected additional resonances have been found in the experimental campaign in case of low target mass. Being aware of the role of the target mass in the acoustical passivity [24] right in the same frequency range as the unexpected resonances, authors have reasons to believe that the loss of acoustical passivity is behind such unexpected behaviour of the nonlinear resonator after the fundamental jump. The experimental campaign will continue toward the investigation of both passivity and absorptive performances of our non-*Linear-Time-Invariant* absorbers, by an ad-hoc conceived test-rig, as the ones proposed in [34], [35], to fully characterize the multi-harmonic scattering field. Numerical and experimental analyses are foreseen to verify the Nonlinear Energy Sink capabilities of our electro-active resonator, as well as its optimization, in a *coupled* environment, as done in [36]. Future contributions will analyse the enforcing of other non-*Linear-Time-Invariant* responses of interest. The preliminary results presented in this contribution have indeed opened the doors toward nonlinear programmable boundaries also in acoustics and at low excitation levels, encouraging the cutting edge research in the inverse problem of nonlinear absorbers design for noise suppression and acoustic waves control.

Appendix A Comparing IIR and RTI in linear target dynamics tuning

Below we report the mobilities of the ER controlled by both the IIR and the RTI control strategies with linear target dynamics. In Fig. 30 both the target mass and stiffness are equally varied to half (Fig. 29a) and twice (Fig. 29b) the open circuit values. Fig. 30 and 31 show the single variation of the target mass and stiffness respectively, while Fig. 32 shows the variation of the target resistance term. These results demonstrate the total equivalence of the two strategies IIR and RTI to achieve tunable linear target dynamics.

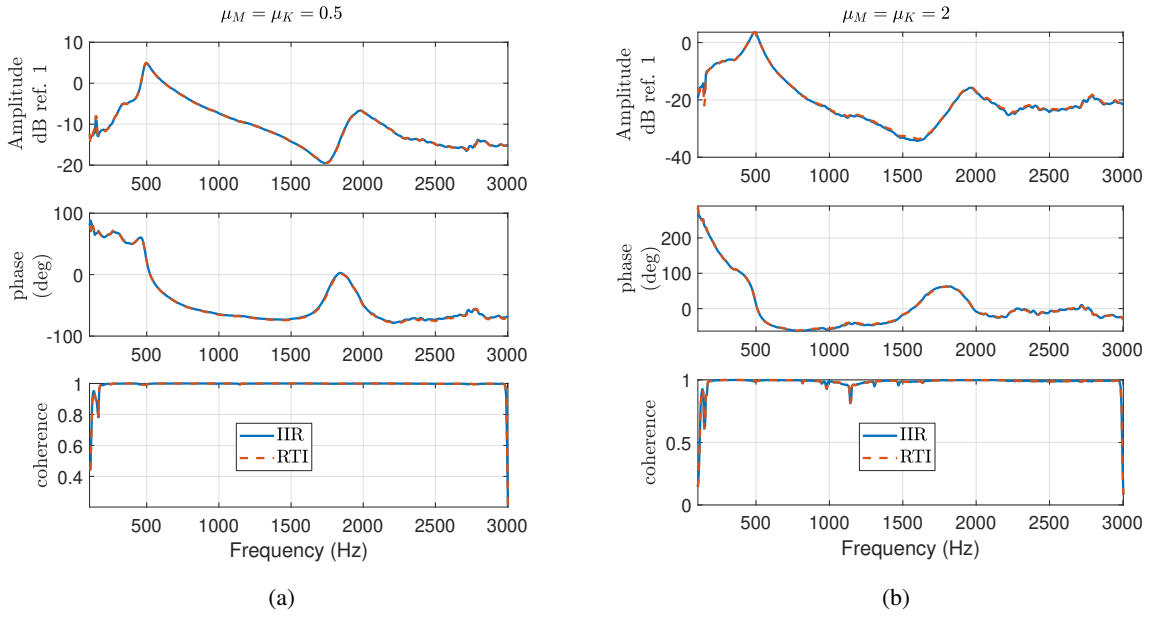


Figure 29: Mobility obtained by targeting a linear SDOF dynamics of the ER with $\mu_M = \mu_K = 0.5$ (a) and $\mu_M = \mu_K = 2$ (b), and $R_{at} = \rho_0 c_0$, by either the IIR (solid blue line) or the RTI (dashed red line).

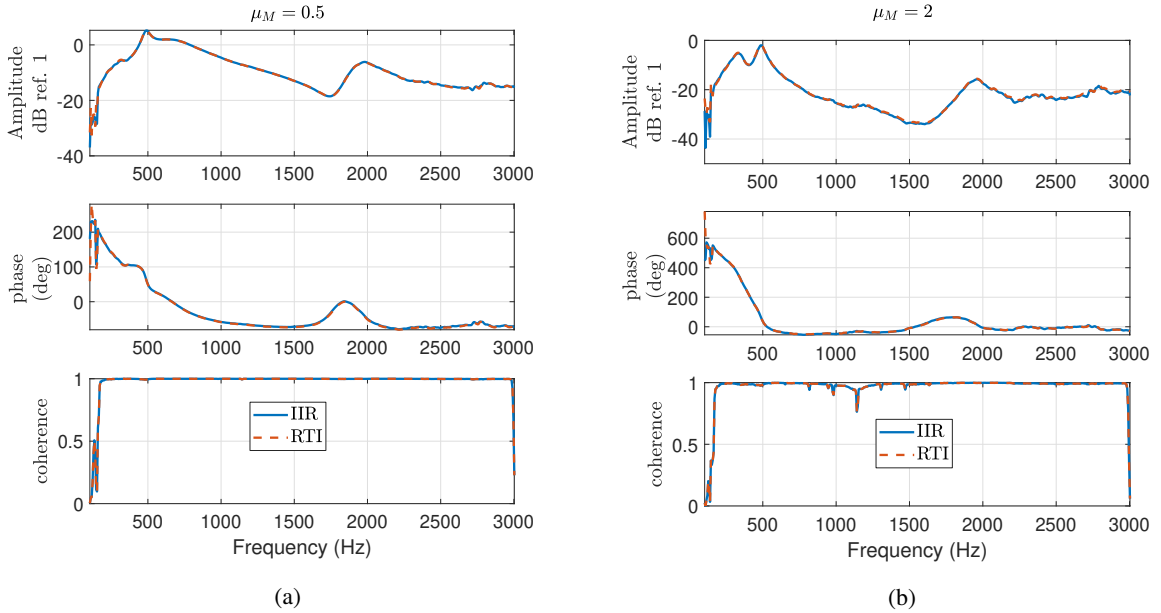


Figure 30: Mobility obtained by targeting a linear SDOF dynamics of the ER with $\mu_M = 0.5$ (a) and $\mu_M = 2$ (b), $\mu_K = 1$ and $R_{at} = \rho_0 c_0$, by either the IIR (solid blue line) or the RTI (dashed red line).

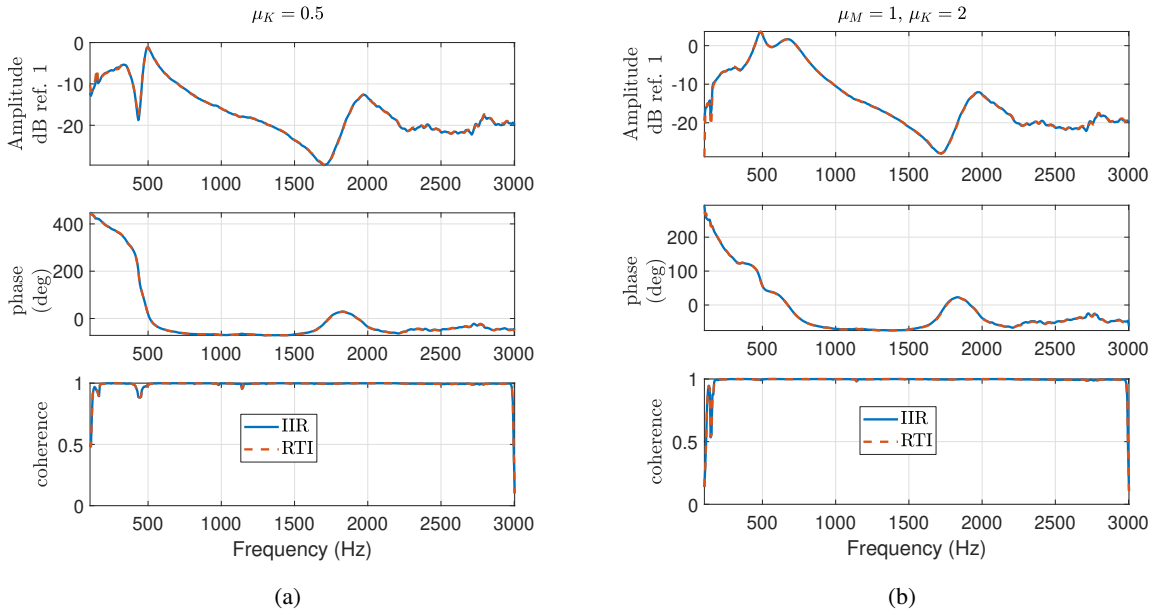


Figure 31: Mobility obtained by targeting a linear SDOF dynamics of the ER with $\mu_K = 0.5$ (a) and $\mu_K = 2$ (a), $\mu_M = 1$ and $R_{at} = \rho_0 c_0$, by either the IIR (solid blue line) or the RTI (dashed red line).

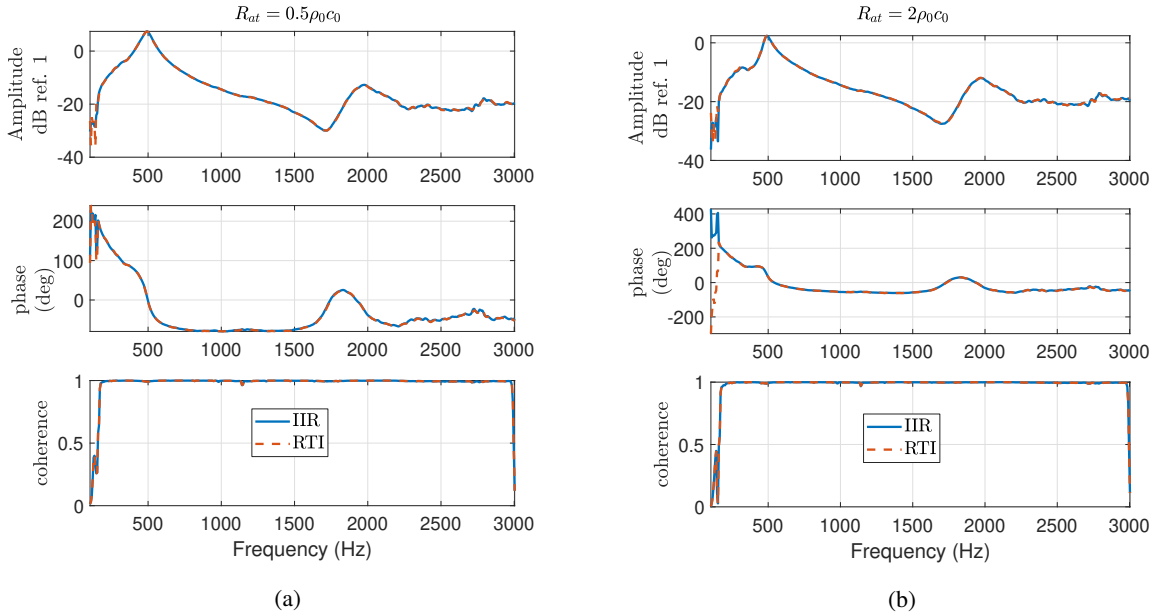


Figure 32: Mobility obtained by targeting a linear SDOF dynamics of the ER with $R_{at} = 0.5\rho_0 c_0$ (a) and $R_{at} = 2\rho_0 c_0$ (a), and $\mu_M = \mu_K = 1$, by either the IIR (solid blue line) or the RTI (dashed red line).

Appendix B Harmonic Balance 1-term solution of the Duffing dynamics in open field.

In this section, we develop the analytical solution of the Duffing target dynamics in open field, obtained by the Harmonic Balance (HB) method with 1-term expansion [30]. Inserting Eq. (9) in (15) in open field, we get the target dynamics equation in open field:

$$2p^+(t) = M_{ad}\ddot{u}_d(t) + (R_{ad} + \rho_0 c_0)\dot{u}_d(t) + K_{ad}\left(u_d(t) + \beta_{NL}u_d^3(t)\right). \quad (17)$$

The excitation $p^+(t)$ is taken as an harmonic function $p^+(t) = p_0^+ \cos(\Omega t)$. In the HB method, the 1-term expansion solution to Eq. (17) is assumed as:

$$u_d(t) = A_1 \cos(\Omega t + \varphi) = A_1 \cos \phi, \quad (18)$$

with $\phi = \Omega t + \varphi$, hence the excitation term can be written as:

$$p^+(t) = p_0^+ \cos(\phi - \varphi). \quad (19)$$

Substituting Eq.s (18) and (19) in Eq. (17), and exploiting the trigonometric identity $\cos^3 \phi = 1/4(3 \cos \phi + \cos 3\phi)$, we get:

$$\begin{aligned} 2p_0^+(\cos \varphi \cos \phi + \sin \varphi \sin \phi) = & -\Omega^2 M_{ad} A_1 \cos \phi - (R_{ad} + \rho_0 c_0)\Omega A_1 \sin \phi \\ & + K_{ad} A_1 \cos \phi + \frac{3}{4} K_{ad} \beta_{NL} A_1^3 \cos \phi \\ & + \frac{1}{4} K_{ad} \beta_{NL} A_1^3 \cos 3\phi. \end{aligned} \quad (20)$$

Neglecting the third harmonic term $\cos 3\phi$ and equating the coefficients of $\cos \phi$ and $\sin \phi$ on the left-hand-side (lhs) and right-hand-side (rhs) of Eq. (20), we get the following 2 equations:

$$\cos \varphi = \frac{A_1}{2p_0^+} \left[-\Omega^2 M_{ad} + K_{ad} \left(\frac{3}{4} \beta_{NL} A_1^2 + 1 \right) \right], \quad (21a)$$

$$\sin \varphi = -\frac{A_1}{2p_0^+} (R_{ad} + \rho_0 c_0)\Omega. \quad (21b)$$

Squaring and summing up Eq.s (21a) and (21b), a quadratic equation in Ω^2 is obtained, with coefficients depending upon A_1 . By quadratic formula, $\Omega(A_1)$, i.e. the amplitude spectrum of the 1-term expansion of $u_d(t)$, is retrieved. This solution is plotted in Fig. 10, comparing it to the fundamental harmonics of the DFT of the time integration of Eq. (17).

References

- [1] P. M. Morse, Some aspects of the theory of room acoustics, The Journal of the Acoustical Society of America 11 (1939) 56–66.
- [2] J. Q. Sun, M. R. Jolly, M. A. t. Norris, Passive, adaptive and active tuned vibration absorbers—a survey, Journal of Vibration and Acoustics, Transactions of the ASME 117(B) (1995) 234–242.
- [3] X. Ma, Z. Su, Development of acoustic liner in aero engine: a review, Science China Technological Sciences (2020) 1–14.
- [4] H. F. Olson, E. G. May, Electronic Sound Absorber, Journal of the Acoustical Society of America 25 (1953) 1130–1136.
- [5] A. J. Fleming, D. Niederberger, S. O. Moheimani, M. Morari, Control of resonant acoustic sound fields by electrical shunting of a loudspeaker, IEEE Transactions on Control Systems Technology 15 (2007) 689–703.
- [6] M. Furstoss, D. Thenail, M. Galland, Surface impedance control for sound absorption: direct and hybrid passive/active strategies, Journal of Sound and Vibration 203 (1997) 219–236.

- [7] D. J. Leo, D. K. Limpert, Self-sensing technique for active acoustic attenuation, in: Collection of Technical Papers - AIAA/ASME/ASCE/AHS/ASC Structures, Structural Dynamics and Materials Conference, volume 4, American Institute of Aeronautics and Astronautics, Reston, Virigina, 1999, pp. 2603–2610. URL: <http://arc.aiaa.org/doi/10.2514/6.1999-1530>. doi:10.2514/6.1999-1530. 558
559
560
561
- [8] E. Rivet, S. Karkar, H. Lissek, Broadband Low-Frequency Electroacoustic Absorbers Through Hybrid Sensor/Shunt-Based Impedance Control, *IEEE Transactions on Control Systems Technology* 25 (2017) 63–72. 562
563
- [9] E. T. J.-L. Rivet, Room Modal Equalisation with Electroacoustic Absorbers, Ph.D. thesis, EPFL, 2016. URL: <https://infoscience.epfl.ch/record/222866>. doi:10.5075/EPFL-THESIS-7166. 564
565
- [10] R. Boulandet, H. Lissek, S. Karkar, M. Collet, G. Matten, M. Ouisse, M. Versaevel, Duct modes damping through an adjustable electroacoustic liner under grazing incidence, *Journal of Sound and Vibration* 426 (2018) 19–33. 566
567
- [11] K. Billon, E. De Bono, M. Perez, E. Salze, G. Matten, M. Gillet, M. Ouisse, M. Volery, H. Lissek, J. Mardjono, Others, In flow acoustic characterisation of a 2D active liner with local and non local strategies., *Applied Acoustics* 191 (2022) 108655. 568
569
- [12] S. Karkar, E. De Bono, M. Collet, G. Matten, M. Ouisse, E. Rivet, Broadband Nonreciprocal Acoustic Propagation Using Programmable Boundary Conditions: From Analytical Modeling to Experimental Implementation, *Physical Review Applied* 12 (2019) 054033. 570
571
- [13] R. E. Roberson, Synthesis of a nonlinear dynamic vibration absorber, *Journal of the Franklin Institute* 254 (1952) 205–220. 572
- [14] I. N. Jordanov, B. I. Cheshankov, Optimal design of linear and non-linear dynamic vibration absorbers, *Journal of Sound and Vibration* 123 (1988) 157–170. 573
574
- [15] S. Aubry, G. Kopidakis, A. M. Morgante, G. P. Tsironis, Analytic conditions for targeted energy transfer between nonlinear oscillators or discrete breathers, *Physica B: Condensed Matter* 296 (2001) 222–236. 575
576
- [16] A. F. Vakakis, O. V. Gendelman, L. A. Bergman, D. M. McFarland, G. Kerschen, Y. S. Lee, *Nonlinear targeted energy transfer in mechanical and structural systems*, volume 156, Springer Science & Business Media, 2008. 577
578
- [17] A. F. Vakakis, Inducing passive nonlinear energy sinks in vibrating systems, *J. Vib. Acoust.* 123 (2001) 324–332. 579
- [18] C.-H. Lamarque, O. V. Gendelman, A. Ture Savadkoohi, E. Etcheverria, Targeted energy transfer in mechanical systems by means of non-smooth nonlinear energy sink, *Acta mechanica* 221 (2011) 175–200. 580
581
- [19] V. Alamo Vargas, E. Gourdon, A. Ture Savadkoohi, Nonlinear softening and hardening behavior in Helmholtz resonators for nonlinear regimes, *Nonlinear Dynamics* 91 (2018) 217–231. 582
583
- [20] B. Cochelin, P. Herzog, P.-O. Mattei, Experimental evidence of energy pumping in acoustics, *Comptes Rendus Mecanique* 334 (2006) 639–644. 584
585
- [21] X. Guo, H. Lissek, R. Fleury, Improving Sound Absorption Through Nonlinear Active Electroacoustic Resonators, *Physical Review Applied* 13 (2020) 014018. 586
587
- [22] G. C. Goodwin, S. F. Graebe, M. E. Salgado, *Control System Design*, volume 27, Prentice Hall New Jersey, 2007. 588
- [23] S. Devasia, Should model-based inverse inputs be used as feedforward under plant uncertainty?, *IEEE Transactions on Automatic Control* 47 (2002) 1865–1871. 589
590
- [24] E. De Bono, M. Collet, G. Matten, S. Karkar, H. Lissek, M. Ouisse, K. Billon, T. Laurence, M. Volery, Effect of time delay on the impedance control of a pressure-based, current-driven Electroacoustic Absorber, *Journal of Sound and Vibration* (2022) 117201. 591
592
- [25] P. Filippi, A. Bergassoli, D. Habault, J. P. Lefebvre, *Acoustics: basic physics, theory, and methods*, Academic press, London NW1 7DX, UK, 1998. 593
594
- [26] L. L. Beranek, T. Mellow, *Acoustics: Sound Fields and Transducers*, Academic Press, Oxford OX5 1GB, UK, 2012. doi:10.1016/C2011-0-05897-0. 595
596
- [27] U. Ingard, *Noise reduction analysis*, Jones & Bartlett Publishers, 2009. 597
- [28] S. W. Rienstra, *Fundamentals of duct acoustics*, Von Karman Institute Lecture Notes (2015). 598
- [29] E. De Bono, Electro-active boundary control for noise mitigation: local and advective strategies, Ph.D. thesis, Université de Lyon, 2021. 599
- [30] A. H. Nayfeh, D. T. Mook, *Nonlinear oscillations*, John Wiley & Sons, 2008. 600
- [31] R. A. Pease, A Comprehensive Study of the Howland Current Pump A Comprehensive Study of the Howland Current Pump Applications for the Howland Current Pump AN-1515, *Most* 29 (2008) 12. 601
602
- [32] J. Steele, T. Green, Tame those versatile current source circuits, *Electronic Design* 61 (1992). 603
- [33] M. Volery, X. Guo, H. Lissek, Robust direct acoustic impedance control using two microphones for mixed feedforward-feedback controller, *Acta Acustica* 7 (2023) 2. 604
605
- [34] H. Bodén, One-sided multi-port techniques for characterisation of in-duct samples with nonlinear acoustic properties, *Journal of Sound and Vibration* 331 (2012) 3050–3067. 606
607
- [35] M. Volpe, R. Côte, S. Bellizzi, Experimental methods for characterization of one port nonlinear acoustic systems: application to sound absorbers, in: *Forum Acusticum*, 2020, pp. 1307–1314. 608
609
- [36] R. Bellet, B. Cochelin, P. Herzog, P.-O. Mattei, Experimental study of targeted energy transfer from an acoustic system to a nonlinear membrane absorber, *Journal of Sound and Vibration* 329 (2010) 2768–2791. 610
611